University of Ioannina
School of Sciences
Department of Physics

Electron spectroscopy using hemispherical and toroidal spectrometers

Master Thesis

Evangelos Savvas Tsiokos

Ioannina, 2024

Ευχαριστίες

Θα ήθελα να ευχαριστήσω τον επιβλέποντα καθηγητή μου, κ. Εμμανουήλ Μπενή για την εμπιστοσύνη που μου έδειξε, αλλά και την υποστήριξη που μου παρείχε, καθώς χωρίς την καθοδήγησή του, η ολοκλήρωση της παρούσας εργασίας θα ήταν αδύνατη. Θα ήθελα επίσης να ευχαριστήσω το Εθνικό Κέντρο Έρευνας Φυσικών Επιστημών (Ε.Κ.Ε.Φ.Ε.) "Δημόκριτος" για τη δυνατότητα διεξαγωγής μέρους των πειραμάτων μας στις εγκαταστάσεις του κέντρου, καθώς και το προσωπικό του Ινστιτούτου Πυρηνικής και Σωματιδιακής Φυσικής (Ι.Π.Σ.Φ.) για την πολύτιμη βοήθειά του κατά την διεξαγωγή των μετρήσεων. Επιπλέον, θα ήθελα να ευχαριστήσω τον καθηγητή Alain Dubois για τους υπολογισμούς του πάνω στη θεωρία 3eAOCC. Ακόμη θα ήθελα να ευχαριστήσω το ερευνητικό κέντρο GSI στη Γερμανία που μας παραχώρησε το τοροειδές φασματόμετρο, ένα πολύτιμο εργαλείο για την έρευνά μας. Τέλος, θα ήθελα να εκφράσω την ευγνωμοσύνη μου στην οικογένειά μου, η οποία, με έχει στηρίξει σε οποιαδήποτε απόφαση έχω πάρει και δεν σταμάτησαν ποτέ να μου θυμίζει να κυνηγάω τα όνειρά μου.

Περίληψη

Το αντικείμενο αυτής της εργασίας είναι ο προσδιορισμός της διπλά διαφορικής ενεργού διατομής των διεργασιών Transfer and Excitation που λαμβάνουν χώρα σε κρούσεις ιοντικών δεσμών O^{7+} (1s) με στόχους αερίων He και H_2. Πρόκειται για ένα σύστημα κρούσης τριών ηλεκτρονίων και τα αποτελέσματα εξετάζονται συγκριτικά με τους υπολογισμούς του μοντέλου IA-RTE, καθώς και με πρόσφατους ab initio υπολογισμούς που έχουν ληφθεί με βάση τη θεωρία 3eAOCC. Τα πειράματα πραγματοποιήθηκαν στον επιταχυντή tandem Van de Graaff 5.5 MV του ΙΠΣΦ του Ε.Κ.Ε.Φ.Ε. "Δημόκριτος" στην Αθήνα. Επιπλέον, η παρούσα εργασία περιλαμβάνει την περιγραφή της συναρμολόγησης ενός τοροειδούς φασματομέτρου ηλεκτρονίων, της λειτουργίας του και της μελλοντικής του χρήσης.

Abstract

The subject of this work is the determination of the double differential cross section of Transfer and Excitation processes that take place in collisions of O^{7+} (1s) ionic beams with He and H_2 gas targets. This is a three-electron collision system, and the results are critically compared to standard IA-RTE model calculations as well as to recent ab initio calculations obtained within the framework of 3eAOCC theory. The experiments were carried out at the 5.5 MV tandem Van de Graaff accelerator of the INPP of NCSR "Demokritos" in Athens. In addition, the present work includes the description of the assembly, operation, and future use of a toroidal electron spectrometer.

Contents

List of Figures

List of Tables

Chapter 1

Introduction

1.1 Accelerator-based Physics

For many decades, accelerators play a very crucial role in the study of fundamental physical phenomena, helping us to understand the cosmos, from the smallest particle to the entire Universe. Furthermore, accelerators not only benefited the physical society, but humanity as a whole (e.g., cancer therapies).

The first particle accelerators date back to the early 20^{th} century. The initial designs were mainly linear accelerators, or linacs, that used alternating electric fields. Accelerators of this type accelerate particles in a straight line due to these alternating fields. The Cockcroft-Walton accelerator, built in the 1930s at Cambridge University by John Cockcroft and Ernest Walton [11], is one of the very first linear accelerators. It was the first accelerator used for splitting atoms. A picture of the accelerator is shown in Fig. 1.1.

The same period, another physicist named Ernest Lawrence invented a circular particle accelerator, called cyclotron [12]. In contrast to linear accelerators, the cyclotron not only uses alternating electric field to accelerate charged particles, but also uses magnetic field to bend their trajectories. Its ability to accelerate particles multiple times made it the primary accelerator design until 1940s. A picture of the first cyclotron is shown in Fig. 1.2.

Another physicist, Robert J. Van de Graaff, invented an innovative particle accelerator in the early 1930s [13]. The Van de Graaff accelerator used a moving belt to transport electric charges to a high voltage terminal. This way he managed to create a really high electric field. The accelerator achieved energies up to 1 MeV, making it an important tool for nuclear physicist of the time. After the Second Word War, due to the need for higher energies, a new type of accelerator, the Tandem Van de Graaff accelerator, was developed. The accelerator operated differently from common linear accelerators, as it used two or more acceleration steps linked together.

The emergence of cyclotrons and synchrotrons [14], a different type of cyclotron,

Figure 1.1: The Cockcroft-Walton accelerator terminal at the National Museum of Scotland. Taken from [1].

opened the way to higher energies for particle acceleration, enabling relativistic speeds. Synchrotrons use strong magnetic fields and radiofrequency cavities to drive and accelerate particles. This type of accelerator is also an important source for extremely bright X-rays, used in various science fields. The concept of storage rings is also based on synchrotrons. Storage rings accelerate particles using strong magnetic fields that circulate them inside the ring.

Electron Beam Ion Sources (EBIS) and Electron Beam Ion Traps (EBIT) can produce highly charged ions by injecting neutral atoms or ions into intense electron beams, under the presence of high electric and magnetic field [15]. Some of their advantages include their small dimensions and the ability to accelerate high-Z highly charged ions to energies of up to hundreds of KeV/u.

During the last two decades, high-intensity lasers have created a new field, that of laser-based accelerators [16]. These lasers generate enormous electric fields (up to TV/m) due to their ultra-intense pulses. A gas medium interacting with the laser beam, is transformed into bubble-shape plasma waves. The electric field accelerates electrons from the surrounding plasma to relativistic speeds. This process is known as laser wakefield acceleration (LWFA) and occurs over a distance of a few millimeters. A representation of the LWFA process is shown in Fig. 1.3.

Figure 1.2: Donald Cooksey and Ernest Lawrence in front of the cyclotron. Taken from [2].

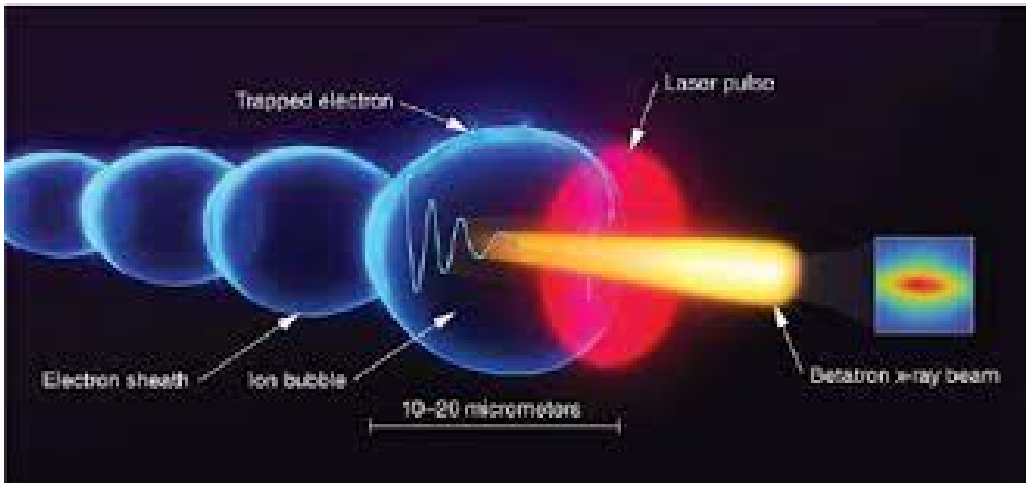

Figure 1.3: Ultra-intense laser pulse races through plasma, accelerating electrons. Taken from [3].

Accelerators have a significant impact on our society. Hospitals have used accelerators for cancer treatment over the last few decades. Proton therapy and carbon ion therapy are very common due to their minimal damage to healthy tissues [17]. Airports around the world ensure flight safety by checking baggage using techniques based on accelerator physics [18]. Additionally, food companies utilize accelerator applications for food sterilization [19].

1.2 Electrostatic Spectrometers

There are several methods to measure the kinetic energy distribution of a charged particle beam. The simpler one is a retarding electric field applied along the beam path [20]. This way, particles having kinetic energy less than the retarding potential difference multiplied by the particle's charge cannot pass this field. If the retarding potential difference changes, the current measured behind the field region also varies,

resulting in the kinetic energy distribution. However, this method does not provide high resolution.

Another method for measuring kinetic energy distribution involves deflecting particles in electromagnetic fields. Electrostatic fields are preferred for this technique because they are easier to handle. Only for high-energy beams magnetic analyzers are preferred. There is a wide variety of electrostatic analyzer designs since any possible electrostatic system with curved optic axis acts like energy analyzer.

A large class of analyzers are the sector field energy analyzers. A common type of this class is the *cylindrical deflector*, made up of two coaxial cylindrical conducting surfaces. A 127.3°deflecting electrostatic sector field analyzer was the first one proposed for analyzing kinetic energies of electron, by Hughes and Rojansky [21]. The main problem of this design are the fringing field effects, especially on the non-dispersive direction.

Other common designs of this class are the *spherical deflector* and *toroidal deflector*. The main advantage of these two deflectors, compared to the previous one, is their ability to focus in both directions. In order to achieve this, deflector's electrodes must be curved, creating this way a toroidal or spherical field. The toroidal sector field was first proposed by Ewald and Liebl [22]. One of the most widely used designs is the *hemispherical analyzer*, designed by Purcell [23].

Another way for creating toroidal electrostatic field distribution, in the vicinity of the optic axis, is adding some flat electrodes between the two cylindrical deflecting electrodes. These electrodes called *Matsuda plates* after the scientist who proposed these [24]. This design is technically easier than toroidal or spherical analyzers. The main disadvantage of this type is the large third-order geometric aberration caused. To solve this problem, the two plates have to be splitted into at least three parts.

Also, more than one electrostatic sector fields can be arranged consecutively, creating an overall achromatic system. The resolving power of the above deflector types can be increased by retarding the charged particle beam before entering the analyzer. The different types of sector field analyzers are shown in Fig. 1.10.

Sometimes, the energy of the charged particles does not remain constant along the circular optic axis. In this case sector field energy analyzers are not the appropriate analyzers. Mirror-type electrostatic energy analyzers work better on fields where the particles are retarded and then accelerated again. Although mirror-type analyzers have smaller dispersion to magnification ratio compared to sector field analyzers, they seem to have some strong advantages. For example, they provide higher order of focusing and larger spatial acceptance.

One of the simplest designs for a mirror-type energy analyzer is the *planar mirror analyzer*. Two parallel planar electrodes form 1D homogeneous field. Particles enter into the analyzer and then exit the analyzer through two narrow slits. Planar analyzers have to be long enough to analyze a wide energy range. A *hyperbolic analyzer* can enlarge the energy range that can be analyzed [25]. This analyzer consists of two flat, vertical to each other, planar electrodes and a hyperbolic one, creating an electrostatic field potential with quadrupole structure.

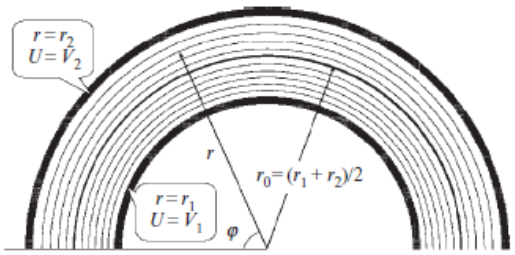

Figure 1.4: cylindrical type

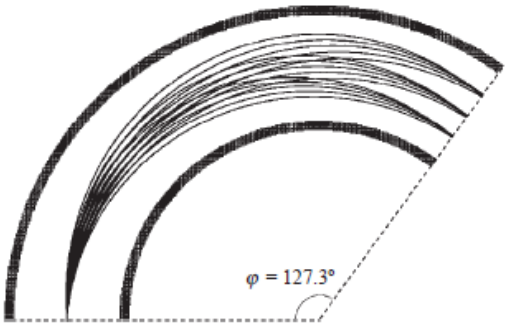

Figure 1.5: cylindrical 127.3°type

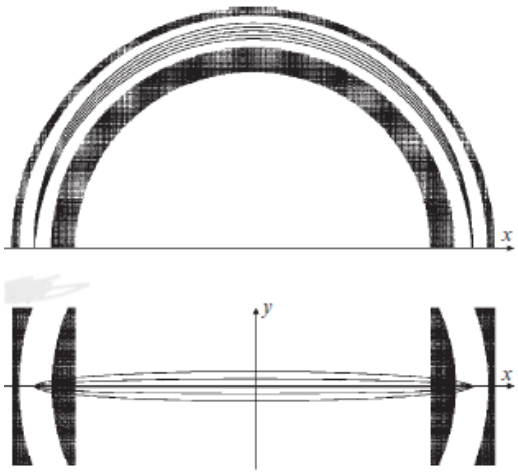

Figure 1.6: hemispherical type

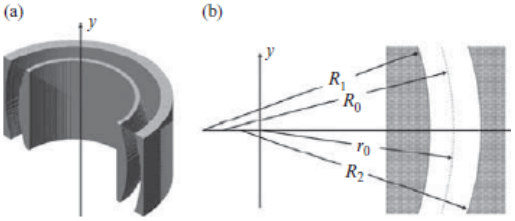

Figure 1.7: toroidal type

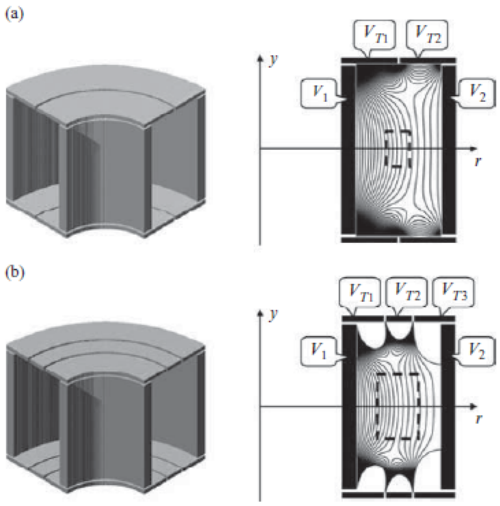

Figure 1.8: deflector with Matsuda plates

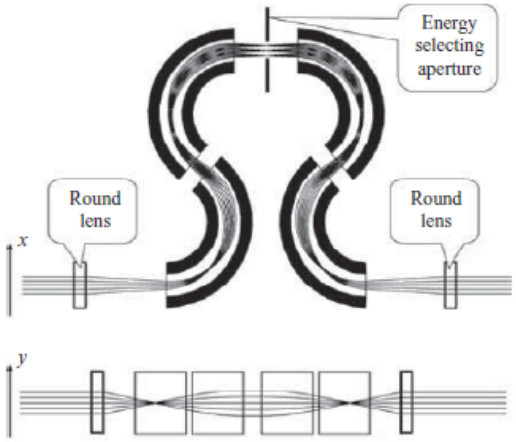

Figure 1.9: achromatic filter

Figure 1.10: Sector field electrostatic energy analyzers types. Pictures taken from [4].

The problem with the above two mirror-type analyzers is the absence of focus action perpendicular to the dispersion plane. Against this problem Zashkvara *et*

al. [26] introduced the *cylindrical mirror analyzer*. Two coaxial cylinders form the electrostatic field and particles injected at the z-axis. This is the most common design until now. There are some other variations, combining two or more cylindrical analyzers, but they are rarely used as they reduce the transition.

Cylindrical analyzers are suitable for a narrow energy scale, just as planar analyzers. That is why Read proposed the *parallel cylindrical mirror analyzer* [27]. In this type of analyzer, the outer cylindrical electrode was replaced by a set of narrow ring-shaped electrodes. In every one of these rings a different potential value is applied. Also this type of analyzer operates well with ions of greater initial solid angle.

Other types of analyzers, like the *box analyzer* [28], provide 2D fields and focus the beam in two perpendicular directions. Four flat electrodes form a rectangular box, elongated at the z-direction. A very interesting idea is the analyzer proposed by Golikov, Davydov and Korablev at 1991 [29]. This analyzer consists of many curved electrodes, playing the role of the equipotential surfaces of the electrostatic distribution. The fine focusing and the high dispersion to magnification ratio makes it appropriate for use especially in small-size spectrometers, despite the complexity in the construction of the electrodes.

Furthermore, some mirror analyzers form 3D field, giving the ability to change the injection angle, like the one proposed by Varga, Tökési and Rajda at 1995. They found that inhomogeneous, in the axial z-direction, rotationally symmetric mirror field can improve the dispersion and focusing quality of the analyzer. Two characteristic examples of this type are the *quasi-conical analyzer* [30] with curved electrode surfaces and the *toroidal mirror analyzer* [31].The first one provides an increased angular acceptance compared to the previous ones or just higher resolving power at a fixed angular acceptance. The second one is almost the same as the parallel cylindrical mirror analyzer and provides axis-to-ring or ring-to-axis focusing. The different types of mirror-type electrostatic energy analyzers are shown in Fig. 1.19.

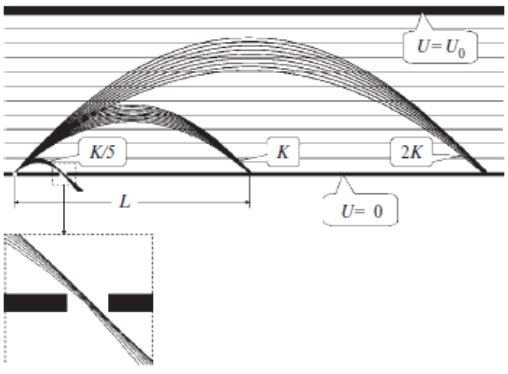

Figure 1.11: planar mirror type

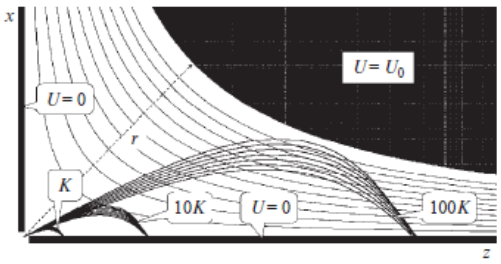

Figure 1.12: hyperbolic field type

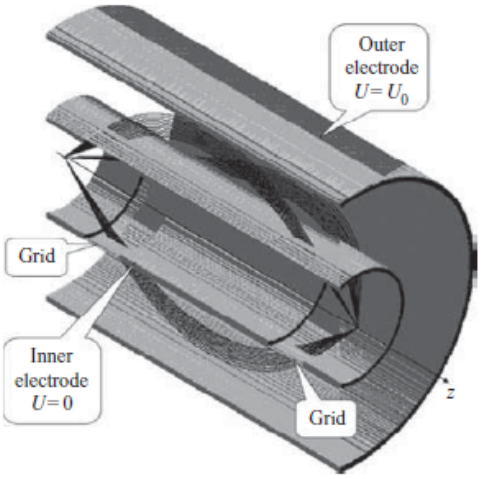

Figure 1.13: cylindrical mirror type

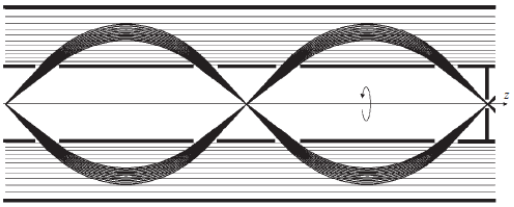

Figure 1.14: parallel cylindrical mirror type

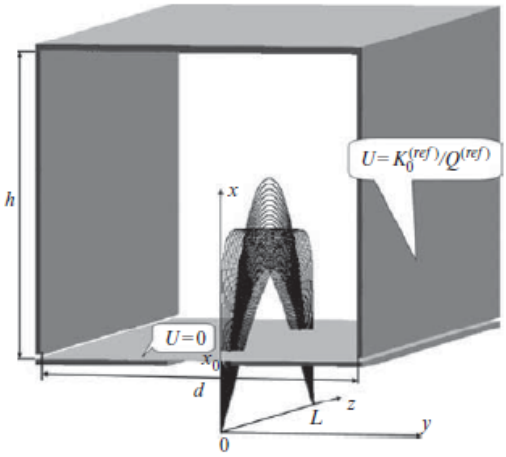

Figure 1.15: box analyzer

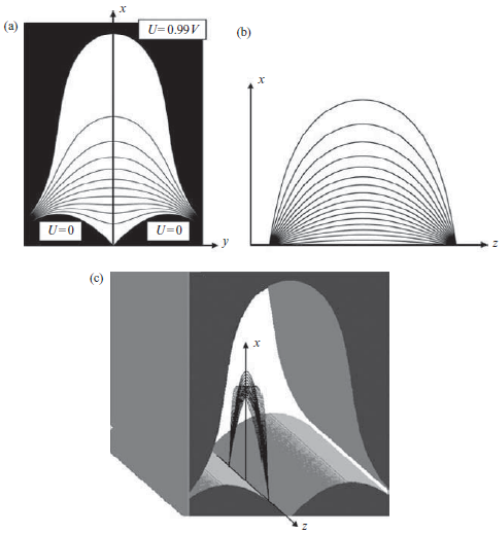

Figure 1.16: ideal focusing analyzer

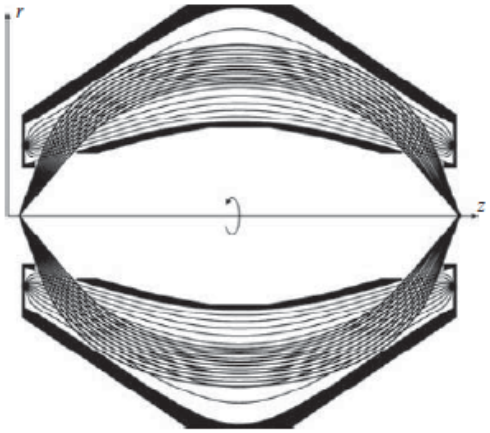

Figure 1.17: quasi-conical analyzer

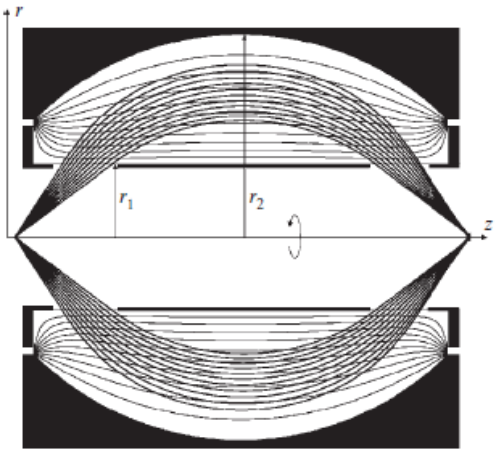

Figure 1.18: toroidal mirror analyzer

Figure 1.19: Mirror-type electrostatic energy analyzers. Pictures taken from [4].

Finally, some analyzers provide energy and angular analysis at the same time. This is simply achieved by recording the energy spectrum in certain direction, but it takes a lot of time and has low angular resolution. Alternatively, using position-sensitive detectors (PSD) can record the energy spectra for different directions. Usually, all axially symmetric mirror-type analyzers with axis-to-ring focusing work also as angular analyzers.

One common type of angular analyzer is the *polar-toroidal analyzer*. Actually, it is a common toroidal deflector, but the particles do not fly in the azimuthal direction but in the perpendicular meridianal direction. The real advantage of this design is the ability to accept disk-like beams. The idea was originally proposed in 1968 by Zashkvara, Korsunskii and Red'kin [32] and one year later by Khokhlov and Remizov [33], but it was the 1982 when Smeenk *et al.* [34] built the first one.

Another analyzer accepting disk-like beams is the *distorted cylindrical mirror field analyzer*, like the one proposed by Trubitsyn [35]. The advantage of this type is that the energy focal line is almost a straight line normal to the z-axis of rotational symmetry of the mirror. Due to several disadvantages, such as the inconvenient positioning of the sample inside, this design is not yet widely used. The different types of energy and angular analyzers are shown in Fig. 1.23.

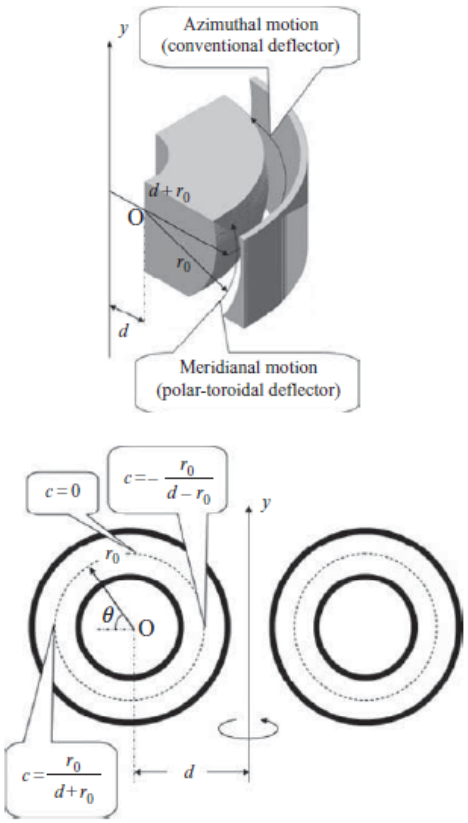

Figure 1.20: polar toroidal analyzer.

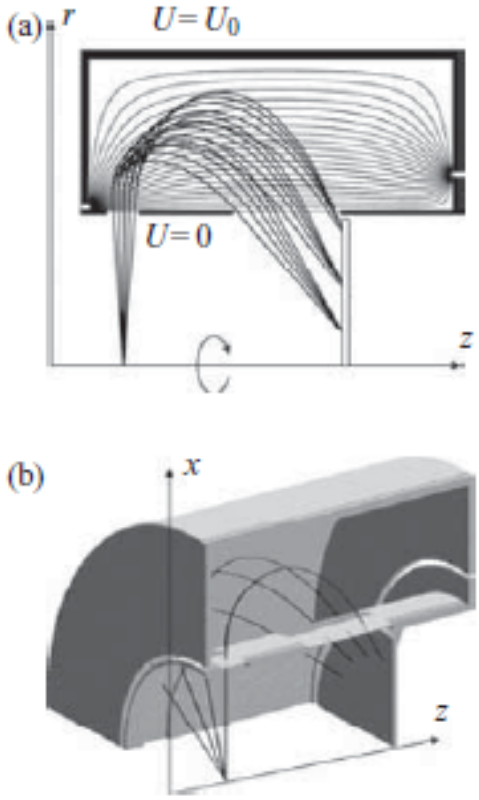

Figure 1.21: mirror analyzer.

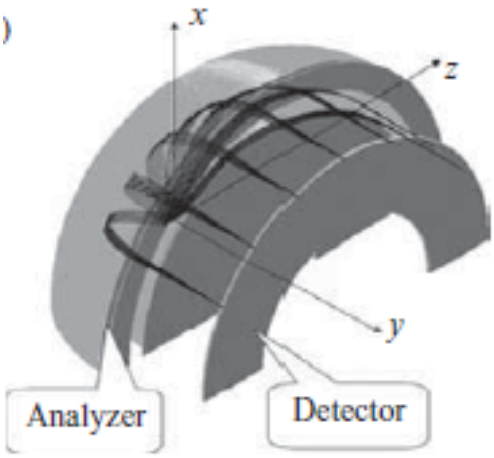

Figure 1.22: transparent view of polar toroidal analyzer.

Figure 1.23: Types of energy and angular analyzers. Pictures taken from [4].

1.3 Thesis Goals

This thesis primarily aims in a systematic study of the mechanisms underlying electron transfer and excitation (TE) in fast ion-atom collisions. Our goal is the

measurement of the double differential cross section (DDCS) for collisions between ionic oxygen beams and gas targets like He and H_2. This results will be examined against the predictions of standard electron scattering model calculations, named IA-RTE, as well as the most recent close coupling theory that involves ab initio quantum mechanical calculations using three active electrons, the 3eAOCC theory.

The secondary aim of this thesis is the preparation of a new toroidal spectrometer recently delivered to the Department of Physics in the University of Ioannina. Our goal is to prepare the spectrometer for operating it either at the Central Laser Facility (CLF) of the University of Ioannina, or at the NCSR "Demokritos".

1.4 Thesis Outline

This thesis is divided into two different parts. The first one concerns the hemispherical spectrograph and the second one the toroidal spectrometer.

In chapter 2 we describe the zero-degree Auger projectile spectroscopy (ZAPS) technique, explaining why this is a powerful tool for high-resolution measurements. After a brief historical review we describe the method and the theoretical background behind the ZAPS technique. We emphasize on the kinematics and the broadening effects affecting our measurements. Moreover in this chapter we give a complete description of how the hemispherical deflector analyzer (HDA) is made and how it works.

In chapter 3, we present in detail the experimental arrangement utilized for our measurements. We introduce the 5.5 MV tandem Van de Graaff accelerator hosted in NCSR "Democritus" in Athens and following we describe the atomic physics experimental setup. Every crucial component of the installation is analyzed, giving an idea of how it was made and work. Furthermore, we describe the process of data analysis. We start with the energy calibration and then explain the process of determination of DDCS from the spectra.

In chapter 4 we introduce the theory behind our experimental work. We start with the Impulse Approximation (IA), a model calculation for ion-atom collisions. After this, we continue with a brief explanation of Binary Encounter electrons. We describe in detail the TE and the main mechanisms underlying it. Finally we describe the 3eAOCC theory, a very promising theory for three-electron systems, like these we work on.

In chapter 5 we present our results on TE measurements. We show the electron spectra recorded in the energy region of 8.5 - 16 MeV for collisions of O^{7+} ground state ion beams with He and H_2 gas targets. We discus our results and compare the experimental data with the IA-RTE model calculations and the 3eAOCC theory predictions.

In chapter 6 we describe the toroidal spectrometer. We analyze the characteristics of every part of the spectrometer, as long as the spectrometer's properties, such as the energy and angular resolution of it. A detailed report on the work done so

far on this new arrangement is also presented.

In chapter 7 the basic principles of operation, as well as the procedure of the installation and characterization of an electron gun is described, including current measurements to find the optimal operation way.

In chapter 8 we present a summary of the results and findings presented at this thesis. We also talk about the future prospects of both experimental setups used for this work. Especially for the toroidal spectrometer, it seems that there are several prospects for further study that will lead to valuable findings.

Part I

The Hemispherical spectrograph

Chapter 2

Zero-degree Auger Projectile Spectroscopy (ZAPS)

Auger electron spectroscopy has been a crucial technique for examining inner-shell vacancy production in energetic ion-atom collisions. This method utilizes light projectiles, like protons or low Z light ions, which barely disturb the outer electron shells of the atom. As a result, the Auger spectra from these collisions is mainly characterized by singly ionized systems [36]. Projectiles with higher nuclear charges can be used, but there is a significant increase in outer-shell ionization, which becomes more intense with heavy projectiles. In this case all outer-shell electrons can be ionized in a single collision, giving complex Auger spectra with numerous satellite lines [37].

A slightly different method, known as Auger electron projectile spectroscopy, provides significant benefits for studying energetic ion-atom collisions [38]. This technique utilizes highly ionized ion beams in a pure charge state. Light target atoms collide with ion beams and excite the inner shells of the projectiles, causing the minimum outer-shell ionization or excitation. This way, the outer-shell electronic configurations of the incident ions during inner-shell vacancy production is preserved. Thus, Auger states of various charge states can be examined individually by simply adjusting the charge state of the incident ions. In addition, the zero-degree Auger projectile spectroscopy (ZAPS) technique, in which the emitted Auger electrons from the projectile are detected at zero-degree angle with respect to the projectile beam helps reducing kinematic line broadening [39].

2.1 Auger Spectroscopy Kinematics

Usually, emitted Auger electrons are scattered by projectiles and follow highly complex trajectories that are difficult to describe. However, in the case of energetic collisions, due to beam's high energy, the projectile ions are scattered in small angles making effects like energy loss negligible. So we can safely assume zero degrees angle scattering. Under this assumption, a simple model using vector addition of velocities

suffices to determine the transformation from the projectile frame to the laboratory frame and to address related kinematic effects without taking into account ion-recoil effects.

The velocity $\mathbf{v}$ of the Auger electron in the laboratory frame can be calculated simply by adding the projectile velocity $\mathbf{V_p}$ to the velocity of the electron $\mathbf{v}'$ in the projectile's rest frame. This way, the kinetic energy ϵ of the electron on the laboratory frame becomes ϵ' in the projectile rest frame according to Eqs. (2.1) and (2.2).

$$\epsilon = \epsilon' + t_p + 2\sqrt{\epsilon' t_p}\cos\theta' \tag{2.1}$$

or

$$\epsilon' = \epsilon + t_p - 2\sqrt{\epsilon t_p}\cos\theta, \tag{2.2}$$

where

$$t_p = \frac{1}{2}V_p^2 = \frac{m}{M}E_p = 548.58\frac{E_p(MeV)}{M(u)}(eV) \tag{2.3}$$

is the reduced projectile energy, also referred as *cusp energy*, E_p the projectile's kinetic energy, M its mass and m the electron's mass. A picture explaining the process of velocities transformation is given in Fig. 2.1.

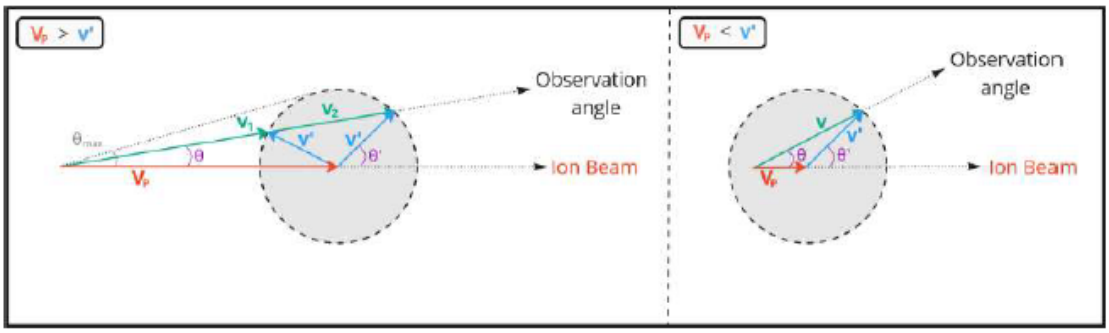

Figure 2.1: Velocity addition diagram showing the projectile velocity $\mathbf{V_p}$, the electron velocity in the laboratory frame $\mathbf{v}$, and the electron velocity $\mathbf{v}'$ in the projectile rest frame. Picture taken from [5].

For convenience, a dimensionless parameter ζ can be introduced to make conversions from rest to laboratory frame [39] as

$$\zeta \equiv \sqrt{\frac{t_p}{\epsilon'}} = \frac{V_p}{v'}. \tag{2.4}$$

Using this parameter, energies for every possible angle can be calculated as

$$\epsilon_{\pm}(\theta) = \epsilon'\left(\zeta\cos\theta \pm \sqrt{1-\zeta^2\sin^2\theta}\right)^2 \quad \text{for } \zeta > 1,\ 0^\circ \le \theta \le \arcsin\left(\frac{1}{\zeta}\right) \tag{2.5}$$

$$\epsilon(\theta) = \epsilon_+(\theta) \quad \text{for } \zeta \le 1,\ 0^\circ \le \theta \le 180^\circ. \tag{2.6}$$

For zero-degree observation, Eqs. (2.5) and (2.6) are reduced to

$$\epsilon_+(\theta = 0^\circ) = \epsilon'(1+\zeta)^2 = \left(\sqrt{\epsilon'} + \sqrt{t_p}\right)^2 \quad (\text{for all } \zeta,\ \theta' = 0^\circ) \tag{2.7}$$

$$\epsilon_{-}(\theta = 0^{\circ}) = \epsilon'(1-\zeta)^2 = \left(\sqrt{\epsilon'} - \sqrt{t_p}\right)^2 \quad (\text{for } \zeta > 1,\ \theta' = 180^{\circ}). \tag{2.8}$$

Eqs. (2.7) and (2.8) highlight kinematic transformation effects that affect both the detection energy of the electrons as well as their differential cross sections. These are:

- Doubling: Two distinct solutions for the laboratory energy ϵ. This means that there are two peaks in the recorded Auger electron spectra that correspond to the same Auger energy.
- Shifting: The energy where an electron is emitted differs for the two frame systems.
- Stretching: The energy width $\Delta\epsilon$ in the laboratory frame is larger than that in the projectile frame.
- Angular Compression: Electrons in the projectile frame are detected within a narrower solid angle compared to that in the laboratory frame.
- Enhancement: The Auger peak's height is larger in the laboratory frame compared to that in the projectile frame.
- Line Broadening Effects: These are additional effects that broaden the energy width of an Auger peak and are due to the geometry detection and the ion's beam energy width.

The above effects can be clearly seen in Fig. 2.2 where the DDCS of the same Auger spectrum is shown in the laboratory and projectile frames. Additionally the above effects are also evident in the electron spectra presented in Chapter 5 and especially in Figs. 5.1 and 5.2. The transformation of the double differential cross section (DDCS) and the single differential cross section (SDCS) results, after taking into account the above effects, as

$$\frac{d^2\sigma}{d\Omega d\epsilon} = \sqrt{\frac{\epsilon}{\epsilon'}}\frac{d^2\sigma}{d\Omega' d\epsilon'} = (1 \pm \zeta)\frac{d^2\sigma}{d\Omega' d\epsilon'} \quad (\theta = 0^{\circ}) \tag{2.9}$$

$$\frac{d\sigma}{d\Omega} = \frac{\epsilon}{\epsilon'}\frac{d\sigma}{d\Omega'} = (1 \pm \zeta)^2\frac{d\sigma}{d\Omega'} \quad (\theta = 0^{\circ}). \tag{2.10}$$

2.2 The Hemispherical Deflector Analyzer (HDA)

The heart of the ZAPS spectrograph is the hemispherical deflector analyzer (HDA). At the entrance of the HDA, a 4-element focusing and deceleration lens system is placed, while at the exit of the HDA a two-dimensional position sensitive detector (2D-PSD) is mounted [40]. The spectrograph, including the gas cell, is

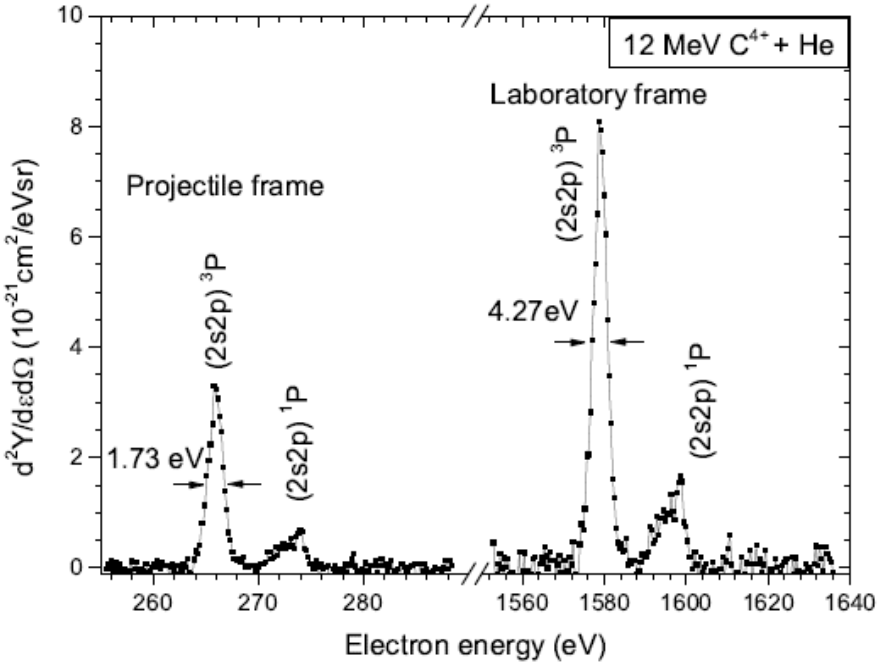

Figure 2.2: Carbon Auger electron spectra obtained in 12 MeV C^{4+} + He collisions as they appear in the laboratory (right) and after transformation to the projectile frame (left). Both spectra have been normalized and energy calibrated, taking into consideration all experimental parameters. The line energy shifting, stretching and enhancement effects in the laboratory frame are clearly seen. Picture taken from [6].

surrounded by a μ-metal shield to minimize the earth's magnetic field. A schematic view of the HDA including the lens system and the 2D-PSD is shown in Fig. 2.3.

The HDA consists of an inner hemispherical plate of radius R_1 and a concentric outer hemispherical plate of radius R_2 as shown in Fig. 2.3. Both HDA and the lens are made of aluminum with their inner surfaces being carbon-coated in order to reduce secondary electrons emission. It is very common in HDAs the entrance aperture to be positioned at the mean radius of the analyzer, $\overline{R} = R_0 = (R_1 + R_2)/2$, and the entrance potential, V_0, to be zero, so that the particle's orbit is circular. But in our HDA the entrance aperture has an offset from the central position while the entrance potential also differs from zero. This is the reason for the HDA to be called *paracentric* [41]. The offset compensates for the fringing fields and thus results in a higher energy resolution.

The detection process is as follows: electrons of charge e, mass m and initial kinetic energy T are ejected far from the spectrograph and at *zero* potential. Before they enter the analyzer, the electrostatic lens focuses them and decrease their kinetic energy from an initial value T to a final value t, for improving the energy resolution.This is done by biasing the HDA on a potential value of V_P, which is the voltage value of the HDA entry electrode V_P (see notation in Fig. 2.3). The final electron energy results as

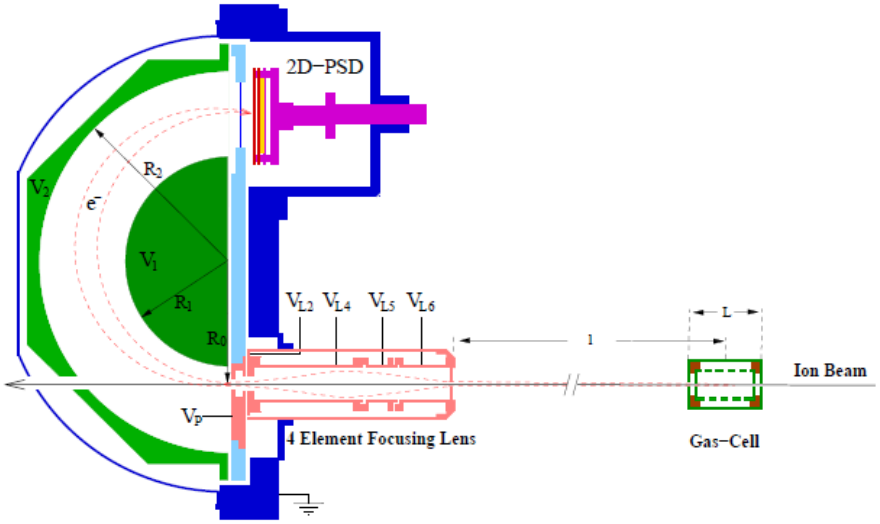

Figure 2.3: Schematic diagram of the hemispherical deflector analyzer including the 4-element focusing lens and 2D-PSD. Taken from [5].

$$t = T - |e|V_p, \tag{2.11}$$

where e is the electron charge.

A schematic representation of the trajectories the particles follow through the lens and the analyzer is given in Fig. 2.4. The electrons enter the analyzer at the entrance point $r_0 \neq R_0$ with a polar angle α and an azimuthal angle β. The azimuthal angle only rotates the motion plane around the optical axis. The polar angle on the other hand affects the energy resolution. As a result, the electrons follow trajectories described by elliptical trajectories $r(\theta)$ that end at r_π, fully deflected through an angle $\Delta\theta = \pi$. These elliptical trajectories are described as [42]

$$r_\pi = -r_0 + \frac{R_0(1+\xi)}{1 + (\xi/\gamma)(1 - \tau\cos^2\alpha^*)}, \tag{2.12}$$

where

- $\xi = R_\pi/R_0$ is the paracentricity of the HDA.
- $\tau = t/w$ is the reduced pass energy.
- w is the pass energy, which is equal to the energy of the decelerated central electron trajectory.
- γ determines the potential at the paracentric entry

$$\gamma \equiv 1 + \frac{|e|V(R_0)}{w}. \tag{2.13}$$

- α^* is the maximum angle of incidence at the HDA entry.

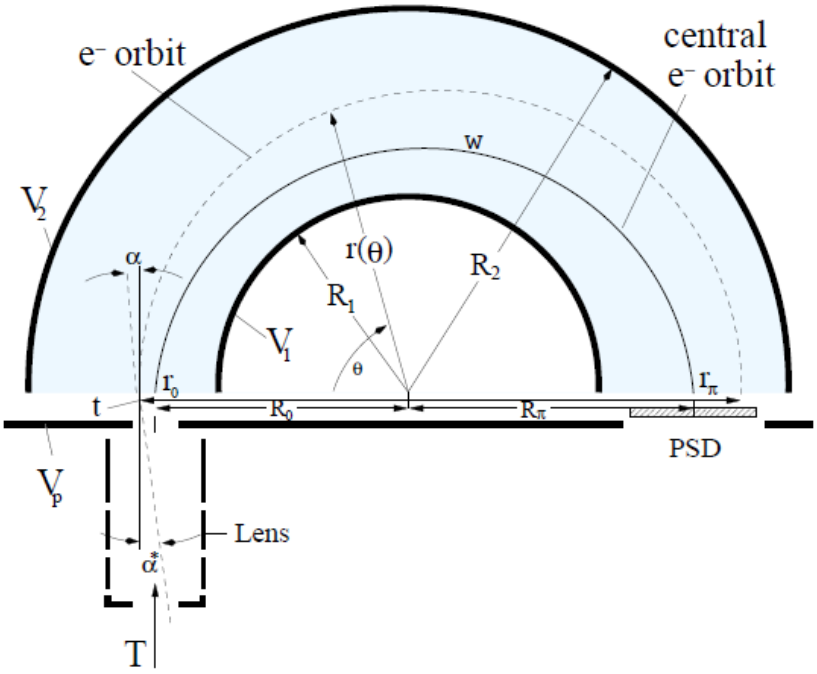

Figure 2.4: Schematic diagram of the HDA geometry and electrons trajectories. Picture taken from [7].

The voltages on the two hemispheres are calculated for the paracentric HDA as [43]

$$-|e|V_{R_i} = \frac{W}{F}\left\{F - \frac{\gamma}{\xi}\left[\frac{R_0 + R_\pi}{R_i} - 1\right]\right\} \quad (i = 1, 2), \tag{2.14}$$

where

- $F = \frac{w}{W}$ is the deceleration factor, that determines the value of plate electrode V_P as
$$V_p = w - W = W\left(\frac{1}{F} - 1\right) \leq 0. \tag{2.15}$$
- W is the tuning energy of the HDA, which is equal to the undecelerated energy of the central electron trajectory.

The base energy resolution R_B for the HDA can be calculated as [40]

$$R_B \equiv \frac{\Delta E_B}{w} = \frac{\Delta r_0 + \Delta r_\pi}{D} + \alpha^{*2}_{\max}, \tag{2.16}$$

where

- Δr_0 is the diameter of the HDA entry aperture. The real diameter is 6 mm, but due to the focusing lens, it is smaller in experimental conditions (virtual aperture).

- Δr_π is the aperture of the exit slit. In fact, this is the spatial resolution of the 2D-PSD, which is 0.15 mm.
- D is the dispersion length

$$D = \frac{R_0 + R_\pi}{\gamma} \cdot \frac{R_\pi}{R_0}. \tag{2.17}$$

In high resolution applications we apply deceleration conditions. In this case the overall base resolution $\mathcal{R}_B$, which is also the actual experimental resolution reads

$$\mathcal{R}_B \equiv \frac{\Delta E_B}{W} = \frac{1}{F}\left(\frac{\Delta E_B}{w}\right) = \frac{1}{F} \times R_B. \tag{2.18}$$

Not all energies can simultaneously be detected at the 2D-PSD but just an energy window. The energy acceptance width corresponds to the base energy width when an exit slit is used. This is different from the case of a PSD-equipped spectrograph. In this case, the effective diameter d_{PSD} defines the energy window ΔT_{window} as [7]

$$\Delta T_{\text{window}} = \frac{d_{\text{PSD}}}{D}\frac{W}{F}. \tag{2.19}$$

All the component of the HDA are shown and explained in Fig. 2.5.

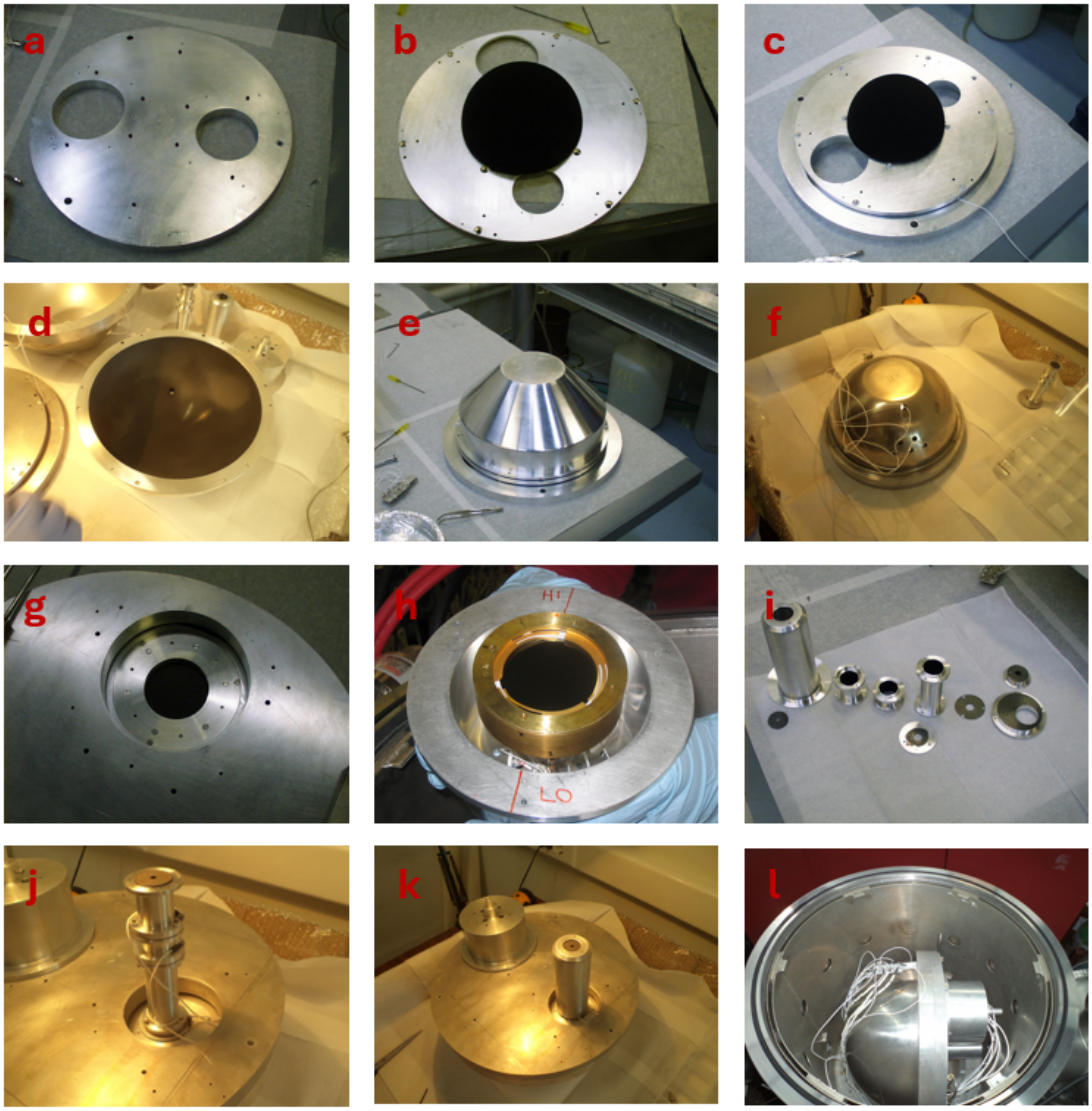

Figure 2.5: [a] Plate V_p. [b] Inner hemispherical electrode V_1 mounted on plate V_p. [c] V_1 and V_p mounted on the ground plate. [d] Outer hemispherical electrode V_2. [e] The HDA with V_1, V_2 and V_p mounted on the ground plate. [f] The HDA with the outer ground plate and cabling. [g] The HDA exit area for the 2D-PSD. [h] The 2D-PSD. [i] The focusing/decelerating lens parts. [j] The lens mounted on the HDA. [k] The HDA fully mounted. [l] The HDA spectrograph mounted inside the vacuum chamber.

Chapter 3

Experimental Arrangement

3.1 The Tandem Van de Graaff accelerator

All experiments were conducted at the 5.5 MV Tandem Van de Graaff accelerator, located at NCSR "Demokritos" in Athens [8], the only laboratory in Greece hosting an ion accelerator. Note that, the accelerator was upgraded recently under the CALIBRA program (Cluster of Accelerator Laboratories for Ion-Beam Research and Applications). A CAD (computer-aided design) view of the Tandem Hall and the beam lines rooms are shown in Fig. 3.1.

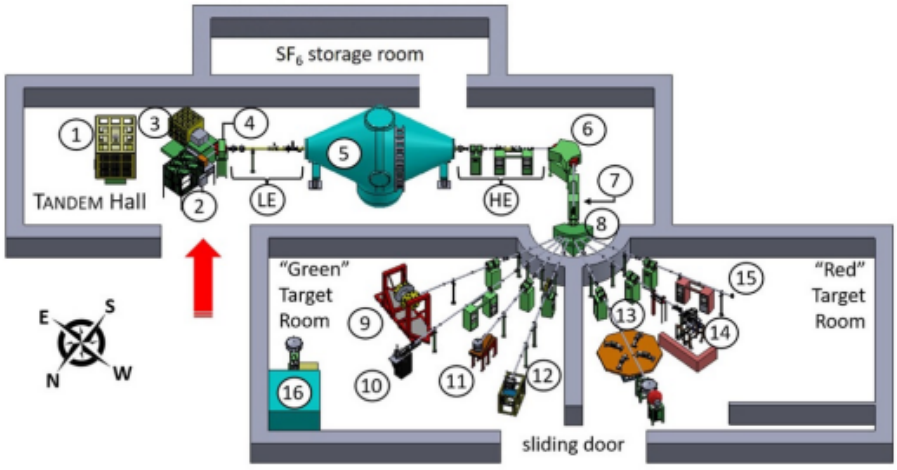

Figure 3.1: CAD view of the TANDEM accelerator facility. (1) Electronics Faraday cage. (2) Duoplasmatron ion source. (3) Sputter ion source. (4) 30° inflector magnet. (5) Tank hosting the generator (terminal). (6) 90° Analyzing magnet. (7) Post-stripper. (8) Switching magnet. (9 - 15) Experimental beam-lines. (16) PAPAP accelerator. Taken from [8].

The acceleration process starts with the formation of the anions. These negatively charged ions are initially formed and accelerated to a few tens of kV in the ion sources (sputter or duoplasmatron). An inflection magnet selects the anions, which next are accelerated towards the accelerator tank due to high potential. The

ions are accelerated until they reach the middle of the tank. There is the terminal stripper, where they collide with either N_2 gas or a thin carbon foil. Depending on the stripping medium we can distinguish two methods, the gas terminal stripping (GTS), or the foil terminal stripping (FTS). Via this process, several electrons can be removed from the anion, producing this way cations of a distribution of charge states. Subsequently these ions are further accelerated, acquiring a kinetic energy at the exit of the accelerator terminal

$$E = (q + 1)V, \tag{3.1}$$

where V corresponds to the maximum accelerator voltage at the center of the tank and q to the ion's charge state.

In order to determine this charge state distribution, we make use of the TADRIS (Transmitted chARge DIStribution) program, which utilizes 4 semi-empirical formulas and also takes into consideration the stripping medium and the ion beam's characteristics. Initial parameters are also the value of the incoming projectile charge state, the projectile's mass (in amu) and its atomic number Z, the energy E (in MeV) and the corresponding velocity V (in mm/ns) [44].

After the formation of the positive ions a dipole magnet, located right after the accelerator's tank, selects the desired ion beam's charge state. This magnet is called "Analyzer". Next, an optional device, called post-stripper, strips the ions to reach higher charge states, that cannot be achieved by Tandem stripping. Finally another dipole magnet, called "Switcher" guides the beam to the various beam lines. As the post-stripper produces higher charge states, the "Switcher" acts like a second "Analyzer".

3.2 The ZAPS experimental setup

3.2.1 The main setup

The beam delivered by the Tandem Van de Graaff accelerator can be delivered to seven different beam-lines. Our beam-line, named L45, is located in the "Red" Target Room and is the only one used for atomic physics. The two main parts of the ZAPS setup are the doubly differential pumped gas cell (GC) and the hemispherical spectrograph. A view of the ZAPS setup, showing every component is depicted in Fig. 3.2.

The distance between the switcher and the chamber is a few meters, thus the presence of a collimation system is required. First, a 4-jaw slits system, known as upstream slits, aligns the ion beam. A following quadrupole magnet focuses the beam at the target area, just before a pair of XY electromagnetic steerers, which finish the tuning of the beam trajectory. About 4.5 meters away from the upstream slits, a last pair of 4-jaw slits system, this time named downstream slits, defines the propagation axis of the beam. A Faraday cup (FC1) placed before the gas cell and along with the BPM system (Beam Profile Monitor) informs us in real-time for the

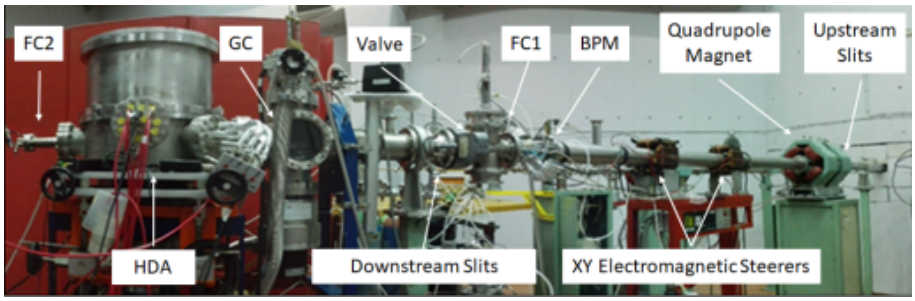

Figure 3.2: The ZAPS setup. Taken from [5].

beam's shape and position. It is used for fine-tuning the beam and maximizing the beam current.

3.2.2 Gas Cell

A valve isolates the gas cell and the HDA from the rest of the beam-line, preventing contamination of the whole Tandem beam-line in case of emergency or during gas cell loading. For the same reason the gas cell is doubly deferentially pumped. In fact, two gas cells coexist, as it shown in Fig. 3.3. The gas target is loaded in the inner one, encompassed in the outer one. An 80 l/s turbo-molecular pump is connected to the outer cell. The double gas cell is enclosed to a stainless steel ISO-160 6-way cross, which is pumped by a 600 l/s turbo-molecular pump. The inner cell is capable of being voltage biased for testing and troubleshooting, but in this case the double gas cell acts as a lens. In this case the setup cannot be used for cross section measurements.

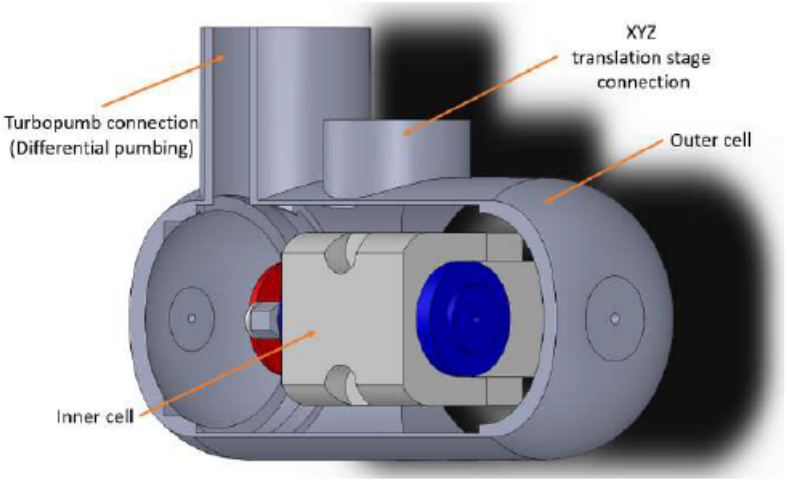

Figure 3.3: CAD view of the gas cell. Picture taken from [5].

When the collision progress takes place, the projectile ion beam collides with the atoms in the gas cell emitting electrons both from the beam and the target. The lens system focuses the electrons, emitted at zero-degree with respect to the ion beam, to the HDA. Before these electrons are recorded by the imaging detector they are analyzed inside the HDA. Due to its high energy, the beam passes through

the HDA and ends up in a Faraday cup. The beam current collected in the Faraday cup (FC2) is measured and used for calibration.

3.2.3 Vacuum manifold

The vacuum manifold consists of 4 turbomolecular pumps and 2 mechanical fore-pumps. At the upstream point of the beam-line, a turbomolecular pump (360 l/s) maintains the vacuum pressure at 10^{-6} Torr. An oil-free mechanical pump supports the turbomolecular pump. The HDA chamber is pumped by a 600 l/s turbomolecular pump. Another same pump maintains the vacuum pressure at the 6-way cross of the gas cell, which is doubly differentially pumped by an 80 l/s turbomolecular pump. These 3 turbomolecular pumps work along with another oil-free mechanical pump. A schematic diagram of the vacuum manifold is shown in Fig. 3.4. Also technical information about the manifold are given in Tab. 3.1.

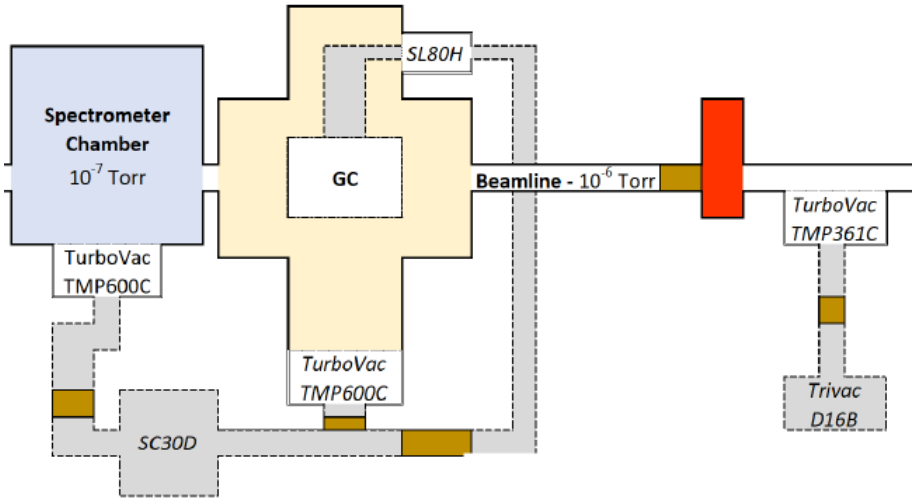

Figure 3.4: Schematic diagram of the vacuum manifold. Picture taken from [7].

Table 3.1: Technical details of vacuum pumps.

Location	Turbomolecular pump	Mechanical pump
Beam-line	TurboVac TMP361C	Trivac D16B
Spectrometer chamber	TurboVac TPM361C	
Gas cell's 6-way cross	TurboVac TPM361C	SC30D
Gas cell	SL80H	

3.2.4 The 2D-PSD detector and data acquisition system

The 2D-PSD consists of a pair of 40 mm diameter chevron style multichannel plates (MCP), acting as particle multipliers [45]. The detector includes also a resistive anode encoder (RAE), which collects the events and determines the exact

particle's position. The channel axis is tilted at an angle of about $\pm 8°$. In this way, electrons collide to the channel's walls producing secondary electrons. The same progress happens on the second plate, after the particles accelerated by an electric field, leading to a cascade effect. A PSD diagram, depicting the multiplication process and the collection of the signal at the four RAE edges is shown in Fig. 3.5.

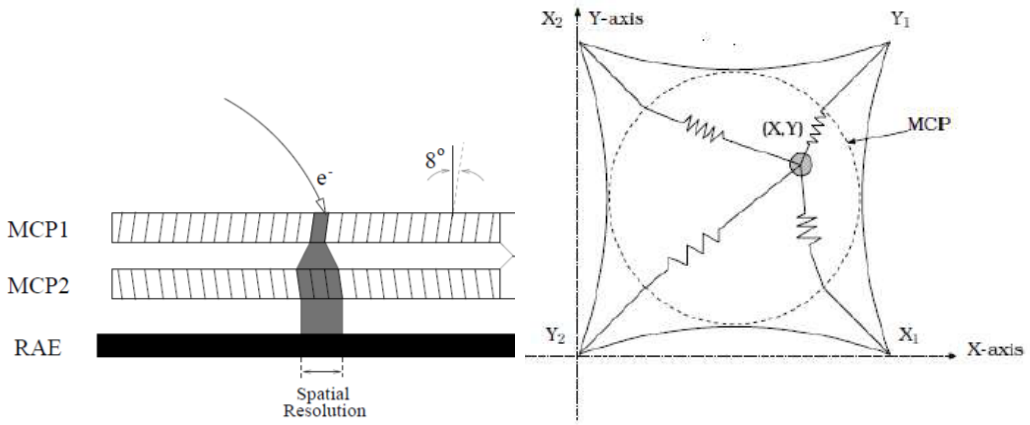

Figure 3.5: [Left] PSD diagram of the two MCPs and the RAE, showing the cascade effect. [Right] Diagram of the RAE showing the signal collection at the four corners. Pictures taken from [7].

Every particle hitting on the anode surface produces 4 electrical signals at the corners of the RAE, creating then 4 pulses. These pulses go through a preamplifier and then, they go through a Digital Signal Processor (DSP) that digitizes them using an Analogue to Digital Converter (ADC). The final product is a 2D image, depicting the exact particle's position. The 2D array XY discretization was set to be 256×256 channels. The X and Y coordinates are derived from Eq. (3.2), where X_1, X_2, Y_1, Y_2 stand for the 4 corners of the RAE as

$$\begin{aligned} X &= \frac{X_1 + Y_1}{X_1 + X_2 + Y_1 + Y_2} \\ Y &= \frac{X_2 + Y_1}{X_1 + X_2 + Y_1 + Y_2}. \end{aligned} \tag{3.2}$$

The data acquisition system has been developed to automatically set the voltages on the spectrograph and then collect the data according to the measurement specifications set by the user. In Fig. 3.6 a snapshot of the data acquisition interface is shown.

3.3 Data Analysis: Determination of Absolute DDCS

The first thing that has to be done in data analysis is to convert the measured electron spectra to DDCS. The process starts with the raw data which depict the number of electron counts as a function of the channel number.

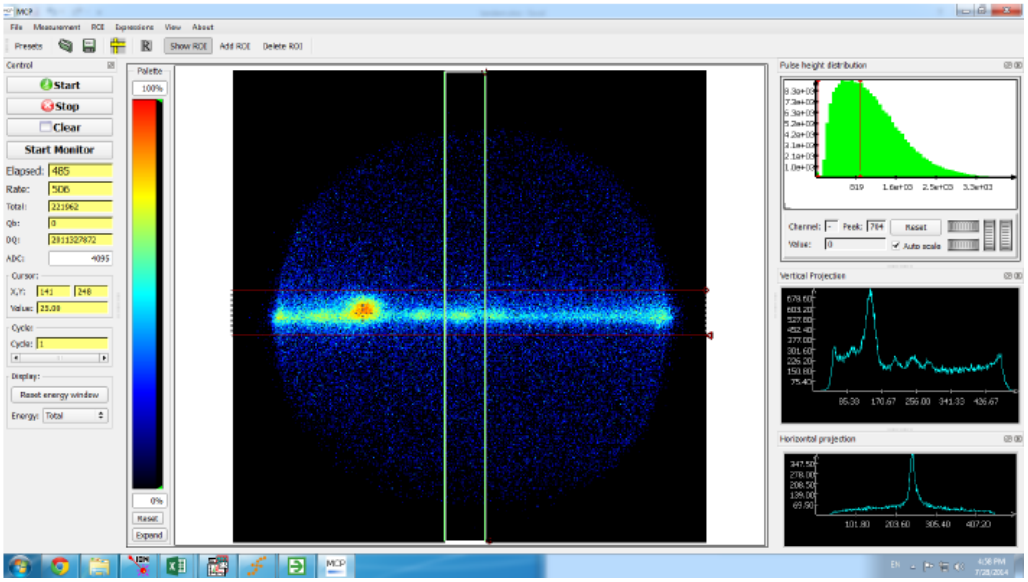

Figure 3.6: The data acquisition interface.

3.3.1 Energy Calibration

As mentioned before, the raw data are recorded per channel number and not electron energy. The conversion of channel number into electron energy involves detecting well-known energy electron peaks from previous experiments. It is important the experimental conditions to be the same in both experiments. There are two possible ways to record well-known electron energies. The first one is using an electron gun and the second one is utilizing well-known Auger lines produced by ion-atom collisions. Electron guns seem to be ideal for calibrations, as they provide a wide energy spectrum and very high accuracy (0.1%). But unfortunately the process is time-consuming. That is why KLL Auger lines are preferred.

The energy calibration procedure requires a quadratic function mapping channel numbers to laboratory frame electron energies, considering the non-linear relationship between them [7]. In the energy calibration process, the first step is to convert the known Auger energies from the rest frame to the lab frame utilizing the reduced projectile energy t_p, along with Eqs. (2.7) and (2.8), which describe the transformation from rest frame to lab frame energies. Once the conversion to lab frame energies is achieved, the center channel for each Auger calibration peak in the lab frame is directly measured from the raw data spectrum. These measured center channels serve as data points for the calibration. The next step is to determine the optimal calibration constants *(a, b, c)*, applying the least squares fit method. It is highly recommended that a minimum of three well-known Auger energy lines is necessary for the least squares fit method to be applicable. This requirement stems from the quadratic nature of the calibration function [7].

$$T(i) = a + b \cdot i + c \cdot i^2. \tag{3.3}$$

As some spectral regions may contain less than three Auger lines the aforementioned calibration method cannot be applied. In this case, the calibration can be

done by repeating the process for various parameters, like elements, beam energy, tuning energy W, or different deceleration factor F. Then, the Eq. (3.3) takes the form

$$T(i) = \frac{W}{F}(A + F - 1) + B \cdot i + C \cdot i^2, \tag{3.4}$$

where:

- $$A = \frac{a}{W}F - F + 1 \tag{3.5}$$
- $$B = \frac{b}{W}F \tag{3.6}$$
- $$C = \frac{c}{W}F \tag{3.7}$$

3.3.2 Double Differential Cross Section

The next step after the energy calibration is the calculation of the double differential cross section. The laboratory DDCS is given by the equation

$$\mathrm{DDCS}_i \equiv \frac{d^2\sigma}{d\Omega dE_i} = \frac{N_{e_i}}{N_I L_c n \Delta\Omega \Delta E_i T \eta}. \tag{3.8}$$

The index i stands for the channel number of the PSD x-projection. It has to be mentioned that Eq. (3.8) does not include a dead time correction (DTC). This factor is the ratio between total counts recorded by a scaler and total counts recorded by the ADC and must be included when the count rate exceeds the capability of the DAQ. In our experiment this does not happen, so the factor can be ignored. The other parameters of the Eq. (3.8) stand for:

- $\boldsymbol{N_{e_i}}$ is the number of electron counts recorded at every channel. The process of counting may involve random effects following Poisson distribution, so there is a statistical uncertainty given by

$$\delta N_{ei} = \sqrt{N_{ei}}. \tag{3.9}$$

- $\boldsymbol{N_I}$ is the number of ions collected at the last Faraday cup during the measurement. The exact number is calculated from the collected charge Q (Eq. (3.10)) divided by the ion beam charge q according to Eq. (3.11), as

$$Q(nC) = \frac{Q_{cnt} I_{FS}(nA)}{C_{nts}} \tag{3.10}$$

$$N_I = \frac{Q(nC)}{q \times 1.6 \times 10^{-10}}, \tag{3.11}$$

where Q_{cnt} is the number of counts collected during a measurement. This number corresponds to the pulses generated by the Beam Current Integrator (BCI) fed to the DAQ, and determines the duration of the measurement. I_{FS} represents the maximum or full scale of the BCI [7].

We assume that the beam current remains unaffected by collisions during the measurements, although this is not entirely accurate. On the one hand, the projectile electron loss processes increase the beam charge, but on the other hand, projectile electron captures decrease the beam's charge. The variation of the beam current during the measurement for a beam passing through a gas of density n and total cross section σ is given by

$$I = I_0 \sigma n L. \tag{3.12}$$

The uncertainty $\frac{\delta N_I}{N_I}$ for usual experimental conditions is less than 5%.

- $\boldsymbol{L_c}$ is the effective length of a gas cell with length L_{gc} and aperture openings D_1 and D_2 and given by

$$L_c = L_{gc} + \frac{D_1 + D_2}{2}. \tag{3.13}$$

The diameter of the two apertures is 0.25 cm and the effective gas cell's length is 5.25 cm. The uncertainty $\frac{\delta L_c}{L_c}$ is less than 5%.

- $\boldsymbol{n}$ denotes the number of molecules per cm^3 and the uncertainty $\frac{\delta n}{n}$ is less than 0.2%.

- Solid angle $\boldsymbol{\Delta\Omega}$ is determined knowing the diameter of the lens entry aperture and the distance between the lens entry and the center of the gas cell and can be calculated as

$$\Delta\Omega(s_0) = 2\pi(1 - \cos\theta) = 2\pi \left(1 - \frac{s_0}{\sqrt{\left(\frac{d_{LE}}{2}\right)^2 + s_0^2}}\right) = 1.50 \times 10^{-4}\,\text{sr}. \tag{3.14}$$

The uncertainty $\frac{\delta(\Delta\Omega)}{\Delta\Omega}$ is less than 2%.

- Energy step $\boldsymbol{\Delta E}$ corresponds to the energy width covered by each channel and can be calculated by taking the first derivative of Eq. (3.3) as

$$\Delta E_i = b + 2c_i \tag{3.15}$$

or according to Eq. (3.4)

$$\Delta E_i = \frac{W}{F}(B + 2C_i). \tag{3.16}$$

The uncertainty $\frac{\delta(\Delta E)}{\Delta E}$ is less than 8%.

- Spectrograph transmission $\boldsymbol{T}$ is determined by the transmission of the three 90% transmission grids located at the front area of the 2D-PSD. Thus the value of T is 0.729. The uncertainty $\frac{\delta T}{T}$ is less than 1%.

- Overall efficiency η results mainly by the MCP absolute efficiency, which is

$$\eta = (50 \pm 5)\,\%, \tag{3.17}$$

  but also form all the other parameters that reduce the detection efficiency. The absolute efficiency is determined by normalizing certain measurements to known experimental or theoretical DDCS.

Both statistical and systematic errors occur in the determination of the DDCS. The overall uncertainty can be estimated employing an error propagation analysis for uncorrelated variables. The mathematical formula describing the systematic uncertainty is given by Eq. (3.18). With the known uncertainties given in previous paragraphs the systematic uncertainty $\frac{\delta\sigma}{\sigma}$ is about 15%.

$$\frac{\delta\sigma}{\sigma} = \sqrt{\left(\frac{\delta N_I}{N_I}\right)^2 + \left(\frac{\delta L_c}{L_c}\right)^2 + \left(\frac{\delta n}{n}\right)^2 + \left(\frac{\delta(\Delta\Omega)}{\Delta\Omega}\right)^2 + \left(\frac{\delta(\Delta E)}{\Delta E}\right)^2 + \left(\frac{\delta T}{T}\right)^2 + \left(\frac{\delta\eta}{\eta}\right)^2} \tag{3.18}$$

Chapter 4

Theory

4.1 Impulse Approximation

The Impulse Approximation (IA) describes the interaction between a very slow target electron and a very fast projectile, without taking into account the collisional effect of the target nucleus. This method has been applied for the first time in 1983 in ion-atom collisions to RTE studies [46] and it was tested successfully in many e-e processes, including e-e excitation [47], e-e ionization [48] and inelastic resonant scattering [49].

The main idea of IA is the much higher projectile velocity V_P, compared to the velocity of the target electron u_t. This way, the electron is considered to be frozen during the collision. From the projectile's rest frame, the electron seems as a quasi-free particle catching up the projectile nucleus with velocity $\boldsymbol{v} = \boldsymbol{V_P} + \boldsymbol{v_t}$. After this, the quasi-free electron impact energy in the projectile frame can be written as

$$\epsilon' = \frac{1}{2}mv^2 = \frac{1}{2}m{V_P}^2 + p_z \cdot V_P + \frac{{p_x}^2}{2m} + \frac{{p_y}^2}{2m} + \frac{{p_z}^2}{2m} \tag{4.1}$$

with $p_j = mu_j$ describing the momentum components in the j directions. For small electron velocities, ${p_j}^2$ terms can be neglected. Adding the ionization energy of the active electron E_i as a correction, Eq. (4.1) can be written as

$$\epsilon' = \frac{1}{2}m{V_P}^2 + p_{z_i} \cdot V_P + \frac{{p_{z_i}}^2}{2m} - E_{Ii}. \tag{4.2}$$

In the IA picture, the DDCS in the projectile frame can be correlated with the SDCS as

$$\frac{d^2\sigma(\epsilon', \theta')}{d\Omega' d\epsilon'} = \sum_i \left(\frac{d\sigma(\epsilon', \theta')}{d\Omega'}\right)\left(\frac{n_i J_i(Q_I)}{V_P + Q_i}\right), \tag{4.3}$$

where

$$Q_i \equiv p_{z_i} = \sqrt{2}\sqrt{\epsilon' + E_{Ii}} - V_P \tag{4.4}$$

and

$$J_i(Q_i) = \iint dp_{x_i}\, dp_{y_i} |\Psi_i(\mathbf{p}_i)|^2 \tag{4.5}$$

is the Compton profile, describing the probability of finding a specific target electron i with z-momentum component Q_i, and Ψ the electron wavefunction in momentum space.

4.2 Binary Encounter electrons

The interaction of a target electron with the projectile in hard binary collisions is one of the most important ionization mechanisms in energetic ion-atom collisions. The heavy projectile nucleus is the Coulombic center, which transfers all of its momentum to the target electron. On the other side, the target is responsible only for the initial electron distribution, as the target's nucleus does not play any crucial role to the whole ionization process. Target's electrons emerging from the collisions are referred to as *Binary Encounter electrons (BEe)*.

The spectroscopic signature of these electrons is a broad energy peak on the spectrum, whose shape denotes the initial electron velocity distribution corresponding to the target's Compton profile [50]. BEe peak can be found at an electron energy ϵ

$$\epsilon_{BE} = 4tcos^2\theta, \tag{4.6}$$

where ϵ denotes the BEe energy, θ is the electron emission angle and t is the cusp energy given by Eq. (2.3). For 0° the BEe energy is $4t$. In the case of a free electron colliding with a bare nucleus of charge Z_p the single differential cross-section can be described by the Rutherford scattering model as

$$\frac{d\sigma(\epsilon', \theta')}{d\Omega'} = \left[\frac{Z_p}{4\epsilon' \sin^2\left(\frac{\theta'}{2}\right)}\right]^2. \tag{4.7}$$

For 0° laboratory electron detection and light targets like He or H_2 the BEe DDCS can be described within IA as

$$\frac{d^2\sigma(\epsilon', \theta' = 180°)}{d\Omega' d\epsilon'} = \left[\frac{Z_p}{4\epsilon'}\right]^2 \sum_i \frac{n_i J_i(Q_i)}{V_p + Q_i}. \tag{4.8}$$

Understanding the BEe production is useful not only for the dynamics of small impact parameter collisions, but also for the study of K-Auger electron spectra in heavy ion collisions. BEe play a crucial role in these spectra and interfere with processes like the Resonant Transfer and Excitation followed by Auger decay discussed below. In our study, BEe peak was used for normalizing the Auger electron spectra, and thus determining the absolute efficiency η of the measurement, resulting in the determination of DDCS.

Until the 90's, the BEe formation in energetic bare-ion-atom collisions was well understood and the use of energetic bare projectiles established the well-known

scaling of the BEe DDCS. However, things was not so clear about collisions between non-bare-ions and atoms [51, 52], despite the indication of BEe DDCS scaling. Partially-stripped ions act more like a strong non-Coulomb short-range potential, in contrast with the bare ions. Currently, fast collisions of non-bare ions and atoms are described within the concept of distorted wave approximation theories [53].

4.3 Transfer and Excitation process

Understanding and modeling of the dynamics of many-body quantum systems under intense, ultra-fast perturbations is a significant challenge in physics and especially on the fields of atoms and molecules in the gas phase or in condensed matter [54]. Energetic (MeV) collisions between few-electron ions with atomic targets is one of the best ways to explore such systems. Despite the really short interaction time in such collisions (less than 1 fs) and the complexity of the interplay between the electron-nucleus (e-n) and electron-electron (e-e) interactions, as well as electron exchange effects, there are some simple systems that can be sufficiently understood. This is the case of ion-atom collisions including electron transfer and excitation (TE) [55]. A fully coherent treatment for such cases has in general been lacking.

Electron capture (or transfer), excitation and ionization are some of the main processes that take place during ion-atom collisions. TE is a process between two interacting electrons. The process involves the excitation of a projectile electron and at the same time, the transfer of a target electron to the projectile. After this process, a doubly-excited projectile state is formed. TE is very interesting as it is closely related to the electron-ion collision process of dielectronic capture (DC). In DC an ion captures a free electron. This phenomenon has important applications in plasma cooling [56].

In asymmetric collisions of heavy projectiles with light targets, such as He or H_2, two distinct peaks are typically observed in the TE spectra. These two peaks are a high-energy peak, that corresponds to the mechanism of resonant transfer excitation (RTE) [57], and a low-energy peak, that corresponds to the mechanism of non-resonant transfer excitation (NTE) [55]. Both RTE and NTE mechanisms are shown schematically in Fig. 4.1. These two distinct peak structures have been extensively studied as derived from the many experiments utilizing a variety of different techniques [56, 58, 59].

The RTE peak structure can be described to first order as a one-step mechanism mediated by a two-center e-e interaction (TCee). Seeing it through the IA, it can be modeled as a quasi-free resonant electron scattering analogous to the inverse Auger process [60]. Although the IA describes adequately the relative collisional energy dependence of RTE, is not an ion-atom collision theory. IA relies on an electron impact theory adjusted for the initial energy distribution of the electron according to the momentum distribution (Compton profile) of the target electron.

Contrary to the RTE, the NTE contributions have been interpreted by a sequence of uncorrelated excitation and transfer events. Each event arises from a separate e-n

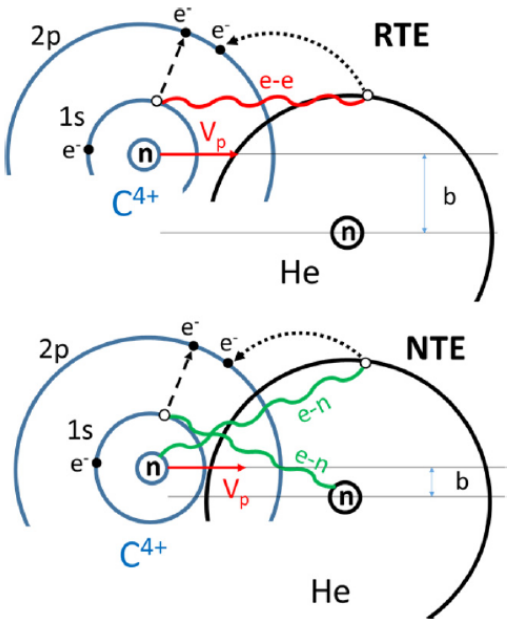

Figure 4.1: Schematic representation of the RTE and NTE mechanisms. Picture taken from [9].

interaction [61]. Both TE mechanisms occur simultaneously during the ion-atom collision and contribute coherently to the production of the same doubly excited projectile state.

All these years, cross sections for these two different TE mechanisms have been computed separately in independent treatments. As a result, their contributions to the total TE cross sections could not be added coherently. These incoherent approaches are not satisfactory and every attempt for a coherent approach has proven problematic. The reason is the presence of many electrons and the interaction between them and the nucleus. Up to now, only two dynamical treatments have appeared in which the signatures of RTE and NTE have been sought. All these treatments involve two-electron collision systems: (i) the two-electron atomic orbital close-coupling (CC) treatment [61], and (ii) the continuous distorted wave four-body (CDW4B) approach [62]. In the new 3eAOCC treatment presented in this thesis both processes are treated for the first time coherently.

4.3.1 Resonant Transfer-Excitation (RTE)

The resonant behaviour of the TE is expressed through the process of RTE, as shown in Fig. 4.2. As mentioned above, RTE is a one-step process mediated by the TCee where the projectile excitation and the transfer of the target electron to the projectile happens simultaneously. RTE process demands the energy of the transferred electron matching the energy of the corresponding Auger, something that happens when the relative impact energy becomes equal to the energy of the corresponding Auger electron. This is the reason why RTE often seen as the time-reversed Auger process.

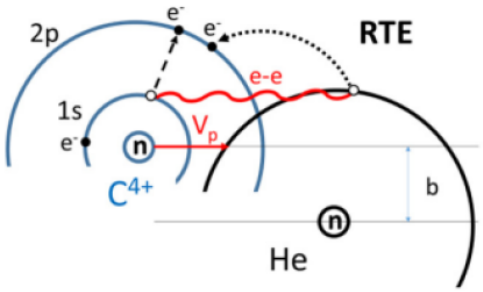

Figure 4.2: Schematic of the resonant transfer-excitation (RTE) process leading to the C^{3+} ($1s2p^2\ ^2D$) level during collisions of C^{4+} ($1s^2$) + He. RTE is a process mediated by a two center electron-electron (e-e) interactions (TCee), indicated here by the red curvy line, leading to the 1s $\rightarrow$ 2p excitation of the projectile electron and the target electron transfer to the projectile 2p indicated by the curved dotted arrow. The projectile velocity V_p and the impact parameter b are also indicated. Taken from [6].

RTE is model by the IA, as a fast enough collision of lightly bound target electrons, considering the incoming target electron as free in the projectile's frame. This happens when $V_p \gg u_t$, where V_p and u_t are the velocities of the projectile ion and the active target electron respectively. With this assumption the target electron is considered a quasi-free particle approaching the projectile along the z-axis with a net velocity $V_e = V_p + u_t$ and a momentum probability distribution given by the Compton profile $J(p_z)$ [63]. The electron impact energy E_e of this quasi-free electron can be written as

$$E_e = \frac{1}{2}m(V_p + u_z)^2 - I = t + p_z \cdot V_p + \frac{p_z^2}{2m} - I, \tag{4.9}$$

where $t = \frac{1}{2}mV_p$ and I the ionization energy of the active target electron. The RTE peak occurs when $E_e = E_A$, for $p_z = 0$ and the collision energy is

$$E_p^{RTE} = (E_A + I) \cdot \frac{M_p}{m}. \tag{4.10}$$

The RTE production cross section in cm^2, within the IA is given by

$$\sigma_{RTE}^{IA} = 2.475 \times 10^{-30} \cdot \frac{(2L_d+1)(2S_d+1)}{(2L_i+1)(2S_i+1)} \cdot \frac{\Gamma_A}{E_R} \cdot \frac{J(p_z)}{V_p + p_z}. \tag{4.11}$$

L_d, S_d and L_i, S_i are terms referred to the orbital and spin angular momentum of the intermediate LS doubly-excited state (d) and the initial projectile state (i), respectively. Γ_A is the Auger transition rate in s^{-1} and E_R the energy in eV of the time-reversed Auger transition.

The relation between RTE cross section and experimental DDCS at 0° is

$$\frac{d\sigma_{RTE}}{d\Omega'}(0°) = \sigma_{RTE}^{IA} \cdot \frac{(2L_d+1)}{4\pi} \cdot \xi, \tag{4.12}$$

where ξ the Auger yield. Light gas targets like He or H_2 are suitable for RTE measurements as their two electrons have narrow momentum distribution, leading to sharp RTE peaks.

4.3.2 Non-resonant Transfer-Excitation (NTE)

NTE mechanism is a sequence of two uncorrelated events occurring at the same time. The one is an electron transfer from the target to the projectile, while at the same time a projectile's electron excitation takes place. Both these processes are independently driven by electron-nucleus (e-n) interactions. The two processes of NTE mechanism are depicted in Fig. 4.3. In this case the process is non-resonant and the NTE appears to be stronger at lower projectile energies than the RTE maximum. In the previous years, NTE has been described in terms of the impact-parameter dependent capture $|P_{cap}(b)|$ and excitation $|P_{exc}(b)|$ probabilities [64] as

$$\sigma_{NTE} = 2\pi \int |P_{cap}(b)||P_{exc}(b)|\, db. \tag{4.13}$$

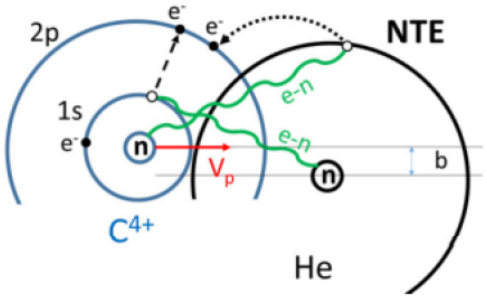

Figure 4.3: Schematic of the non-resonant transfer-excitation (NTE) process leading to the C^{3+} ($1s2p^2\ ^2D$) level during collisions of C^{4+} ($1s^2$) + He. NTE is a process mediated by two electron-nucleus (e-n) interactions between a projectile electron and the target's nucleus together with a target's electron with the projectile's nucleus. Note that these two (e-n) interactions occur independently. The green lines represent the two electron-nucleus interactions, leading to the 1s $\rightarrow$ 2p excitation of the projectile indicated by the straight dashed arrow together with an electron transfer from the target to the projectile 2p indicated by the curved dotted arrow. Taken from [6].

Different experimental techniques of low resolution coincidence measurements, like those of the emitted X-ray and the projectile charge state (RTEX), or of the X-ray and a second X-ray (RTEXX) have been used for investigation of TE process [7]. Another technique is the the high resolution Auger electron spectroscopy RTE followed by Auger decay (RTEA). In fact, RTEA is exact experimental technique utilized in our experiments, as we record the Auger spectra.

RTEX is an ion-atom collision process which is closely related to another process between colliding electrons and ions, the Dielectronic Recombination (DR), where a free electron is captured by an ion. DR is a Radiationless Capture (RC) process

followed by photon emission. The same way, the ion-atom RTEA is closely related to the RC process followed by Auger decay, also known as Resonant Elastic Scattering (RES). These processes are schematically illustrated in Fig. 4.4.

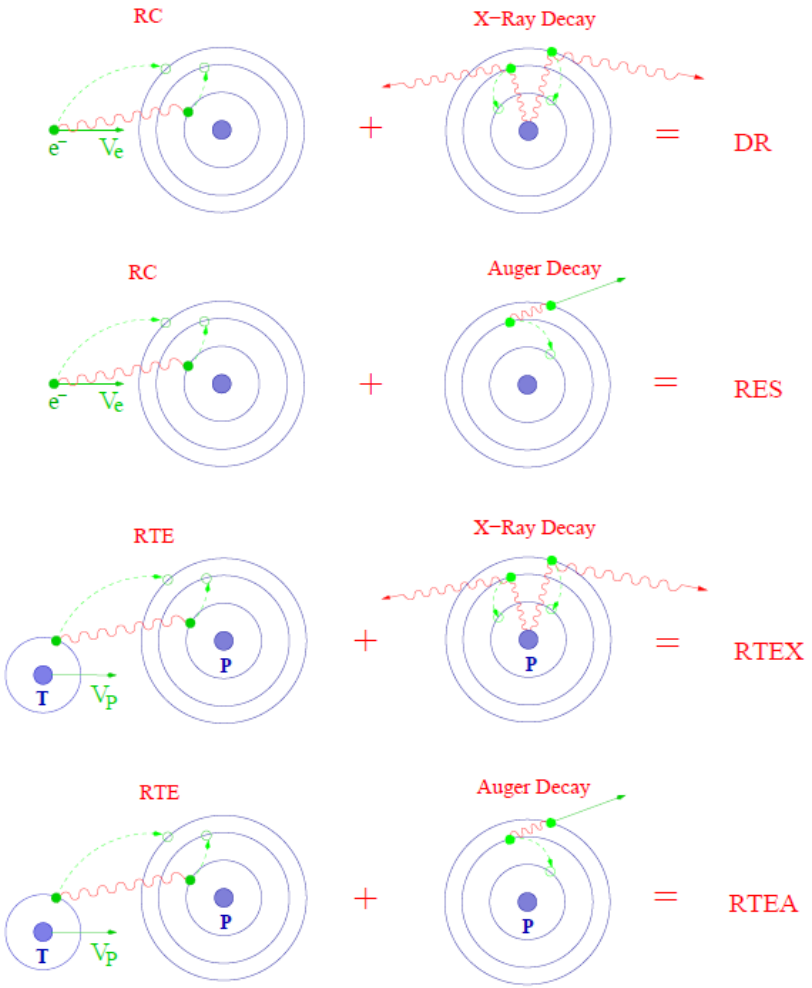

Figure 4.4: Schematic diagram of the Dielectronic Recombination (DR), Resonant Elastic Scattering (RES), Resonant Transfer and Excitation followed by X-ray emission (RTEX) and Resonant Transfer and Excitation followed by Auger electron emission (RTEA). RTEX and RTEA are the ion-atom processes analogous to the electron-ion DR and RES process respectively. Picture taken from [7].

4.4 3eAOCC theory

Many-body quantum systems collisions, with energies of a few MeV, theoretical treatment demands dynamical calculations, involving three active electrons within full configuration interaction theories. Such a theory is the three active electrons atomic orbital close-coupling (3eAOCC) theory. It is a non-perturbative, semi-classical atomic orbital close-coupling treatment with asymptotic descriptions of the atomic collision partners. The time-dependent Schrödinger equation is solved nonperturbatively, taking into account all the couplings related to the static and

dynamic inter-electronic repulsions and effects arising from the Pauli exclusion principle.

Contrary to other theories, the core does not considered to be frozen and much more than one electrons involved in the dynamics. In fact, the atomic center electronic structures described through sets of Gaussian-type orbitals (GTO). Selected antisymmetrized products of them are used for the combination of these states. This way, both ground and excited states for neutral or ionized atoms are described.

This method works very well for He-like and Li-like ions. More specifically, for the helium, the descriptions can be made with a model potential binding only one electron to the He^+. The potential can be described through the equation

$$V(r) = \sum_{i=1}^{13} -\frac{c_i}{r} e^{-a_i r^2}. \tag{4.14}$$

The atomic states centered on He and represented by the potential of Eq. (4.14), He-like and Li-like ions are formulated through sets of GTOs, described as

$$G(r) = N r^l \, e^{-ar^2}, \tag{4.15}$$

where N is a normalization factor.

All the 3eAOCC calculations that are critically compared to the measurements and presented in chapter 5, were provided by Prof. Alain Dubois of the University of Sorbonne.

Chapter 5

Transfer and Excitation measurements

In this section the DDCS Auger electron spectra for TE measurements is presented. The following spectra are produced from collisions of O^{7+} ground state ion beams with He and H_2 gas targets. During the collision He-like $2p^2\,{}^1D$ doubly excited states are formed. These states Auger decay to $1s^2$ ground state producing electrons of characteristic energies. All measurements were taken at 40 mTorr gas cell pressure and with deceleration factor $F = 1$.

The first step was the energy calibration. This can be done through the Eq. (3.3). Having the raw data calibrated, the next step is the calculation of the $DDCS_i$. The $DDCS_i$ is calculated through the Eq. (3.8). Some factors of the Eq. (3.8), like L_c or η remain fixed, while some other like the number of ions, are dynamic. To calculate the N_I we use the equation Eq. (3.10), in which the I_{FS} was 0.5 nA for our experiments. For each beam energy we recorded 10-11 spectra, each one of 5000 counts, with time duration from about 30 minutes, up to 2 hours.

In Fig. 5.1, the Auger DDCS spectra for collisions between O^{7+} and He, in the collision energy region between 8.5-16 MeV, are presented. Additionally, in Fig. 5.2 the same spectra corresponding to the projectile rest frame are presented. The DDCS on the projectile frame can be calculated according to Eq. (2.9) as

$$DDCS_{proj} = DDCS_{lab} \cdot \sqrt{\frac{E_{proj}}{E_{lab}}}. \tag{5.1}$$

The Auger peak of interest is the $2p^2\,{}^1D$, located in the energy region of about 475 eV to 480 eV in the projectile rest frame. This peak is stronger than the other $2l2l'$ peaks.

In Fig. 5.3 the DDCS spectra in the projectile frame in the energy region of interest, are plotted after background subtraction. A third order polynomial fit was used for background subtraction. It is evident that the $2p^2\,{}^1D$ peak shows a resonant behavior gradually increasing up to a point and then gradually decreasing as a function of the collision energy. The maximum value of the DDCS is observed

for the collision energy of 14.80 MeV. Along with the change in the DDCS value, changes in the peak width are also observed since the energy resolution $\Delta E/E$ remains constant for all the measurements.

An interesting finding is the presence of a clear peak at 460 eV for the lowest collision energy $E_p = 8.65$ MeV, absent for the other collision energies. This peak involves a very weak transition from the $2s2p\,^3P$ state. We know the existence of the transition at this energy region, but we are not sure if this peak corresponds to this transition. Unfortunately, the tandem accelerator does not provide adequate currents for lower energies to investigate this peak as well. Moreover, due to a technical problem of the Tandem accelerator we were not able to run experiments at higher energies to fully examine the behavior of the DDCS.

In addition, in our study we included the collisions of O^{7+} ground state ion beams with H_2 gas targets for the energy region of 9.5-16 MeV. The spectra in the laboratory frame and the projectile rest frame are shown in Fig. 5.4 and Fig. 5.5, respectively. The DDCS spectra in the energy region of interest after background subtraction are shown in Fig. 5.6.

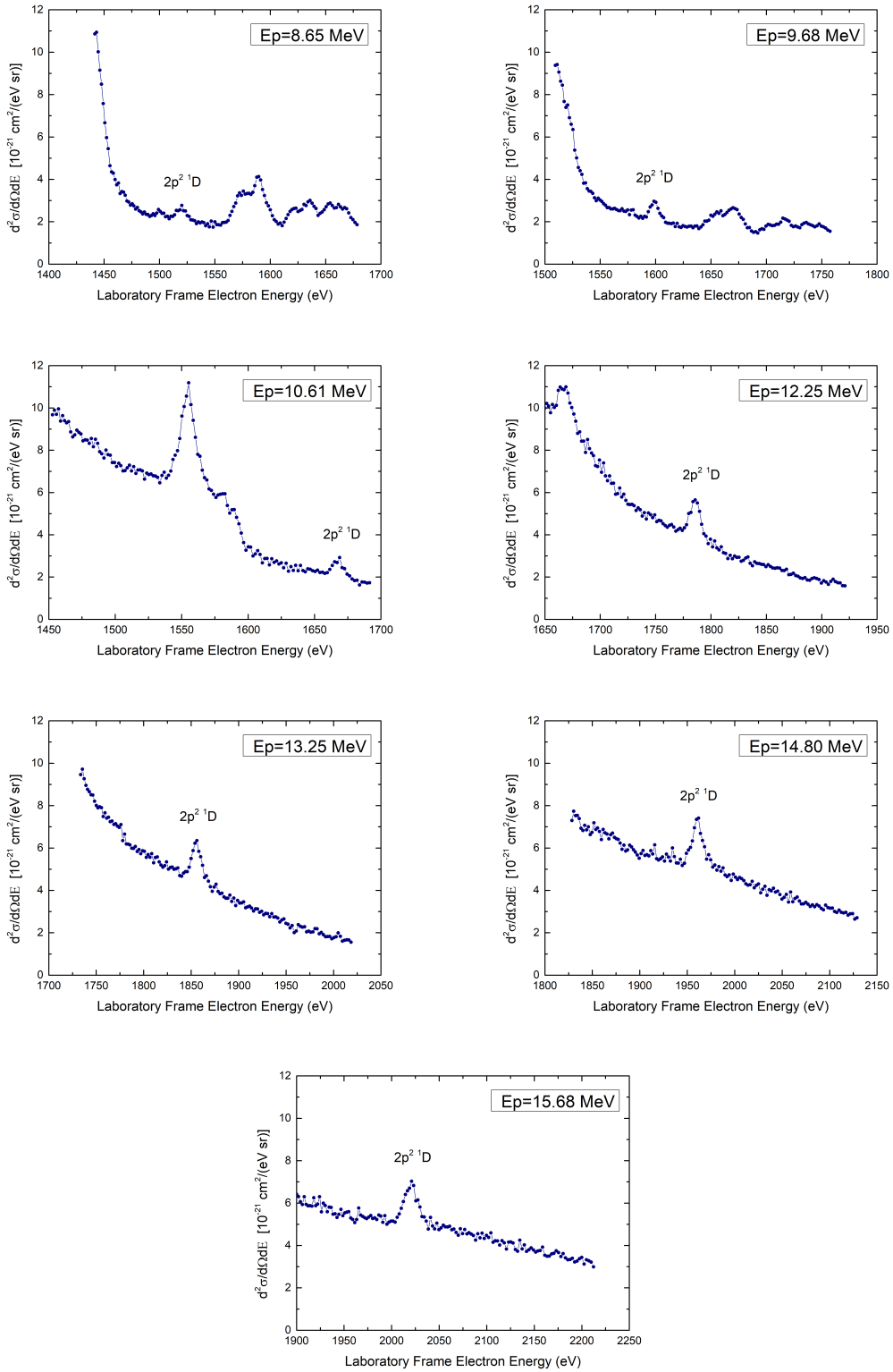

Figure 5.1: Laboratory frame DDCS electron spectra for the collision system of Ep(MeV) $O^{7+}(1s)$ + He. The RTE peak of interest $2p^2\,{}^1D$ is depicted in each graph.

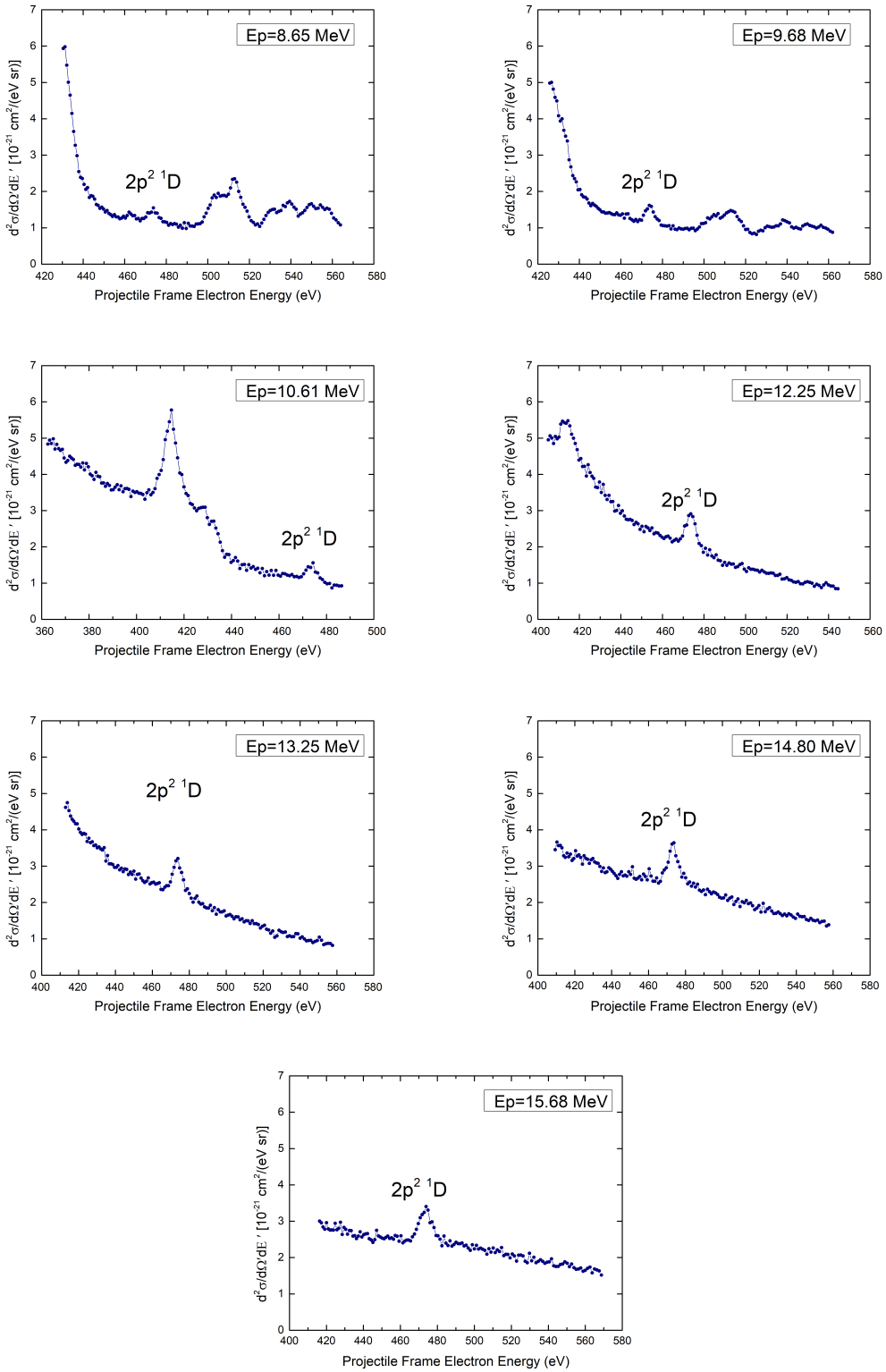

Figure 5.2: Projectile frame DDCS electron spectra for the collision system of Ep(MeV) $O^{7+}(1s)$ + He. The RTE peak of interest $2p^2\,{}^1D$ is depicted in each graph.

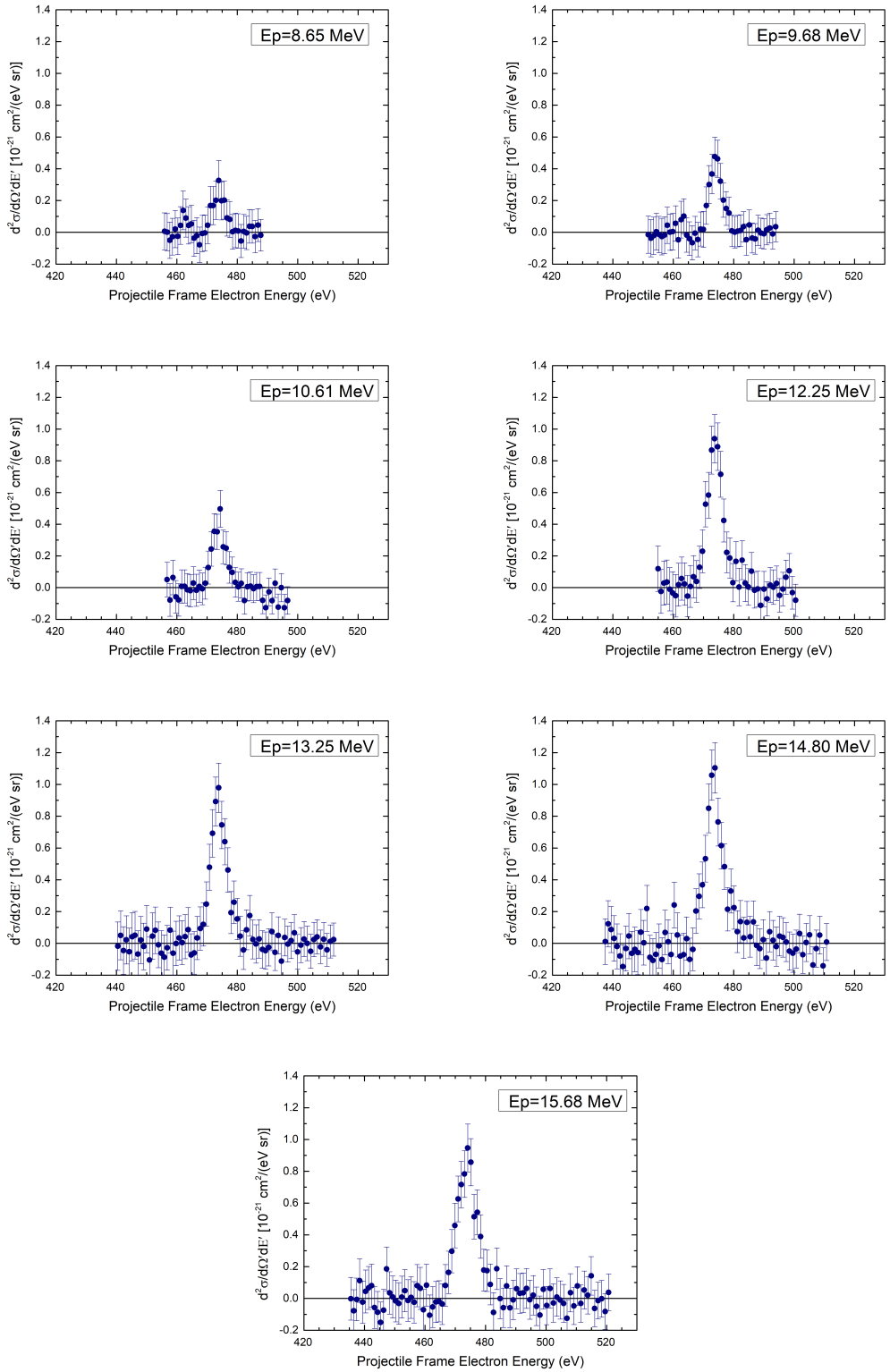

Figure 5.3: DDCS Auger electron spectra (background subtracted) showing the $2p^2\,{}^1D$ RTE peak for the collision system of Ep(MeV) $O^{7+}(1s)$ + He.

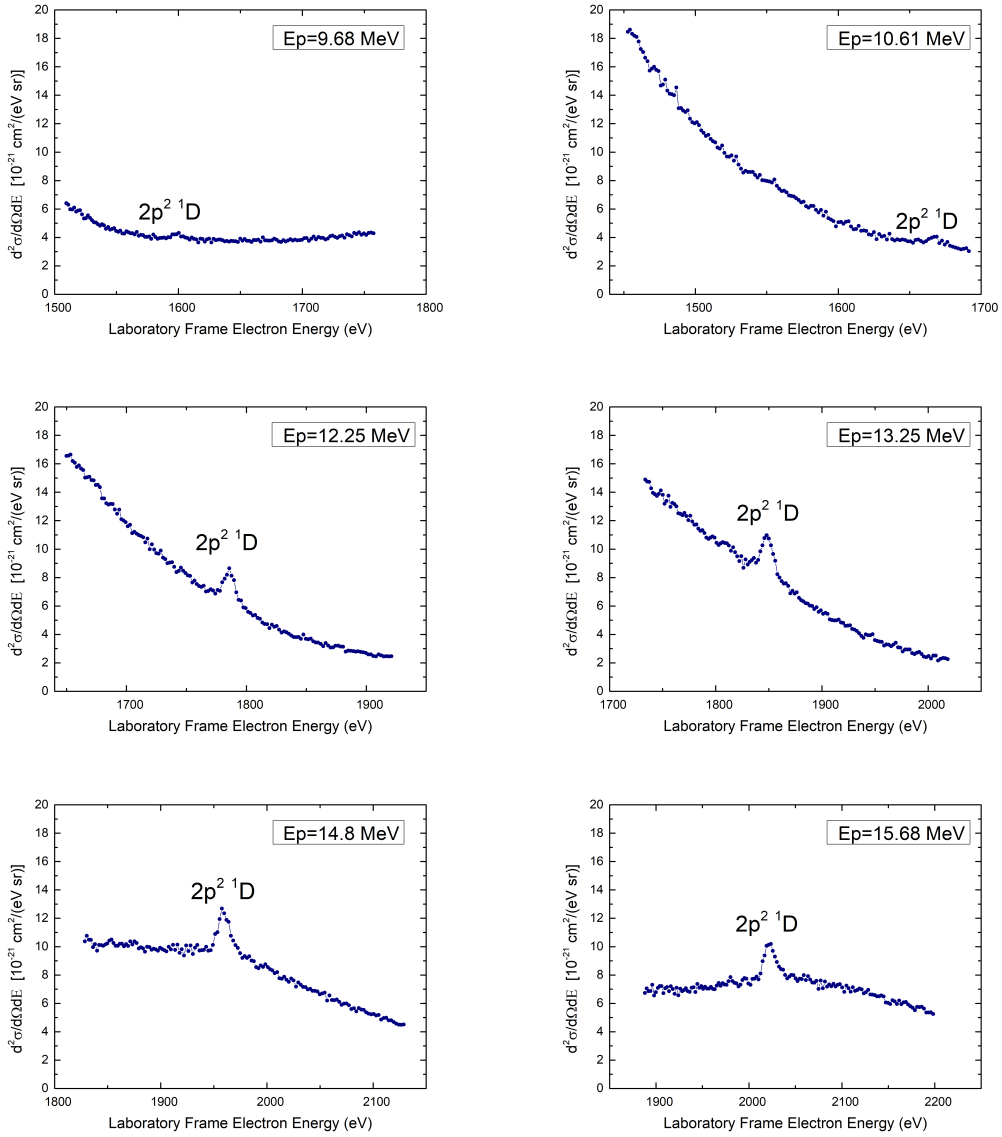

Figure 5.4: Laboratory frame DDCS electron spectra for the collision system of Ep(MeV) $O^{7+}(1s) + H_2$. The RTE peak of interest $2p^2\,{}^1D$ is depicted in each graph.

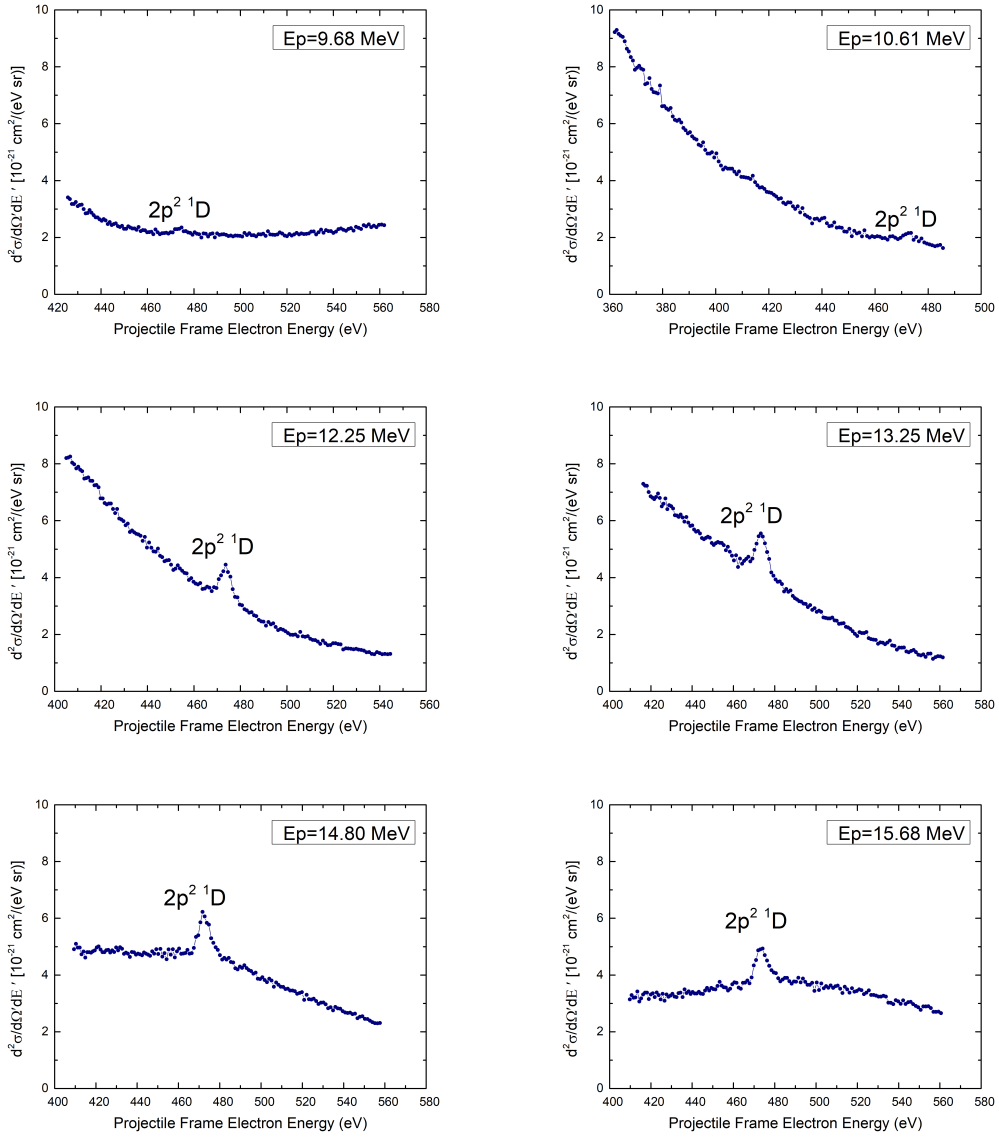

Figure 5.5: Projectile frame DDCS electron spectra for the collision system of Ep(MeV) $O^{7+}(1s)$ + H_2. The RTE peak of interest $2p^2\,{}^1D$ is depicted in each graph.

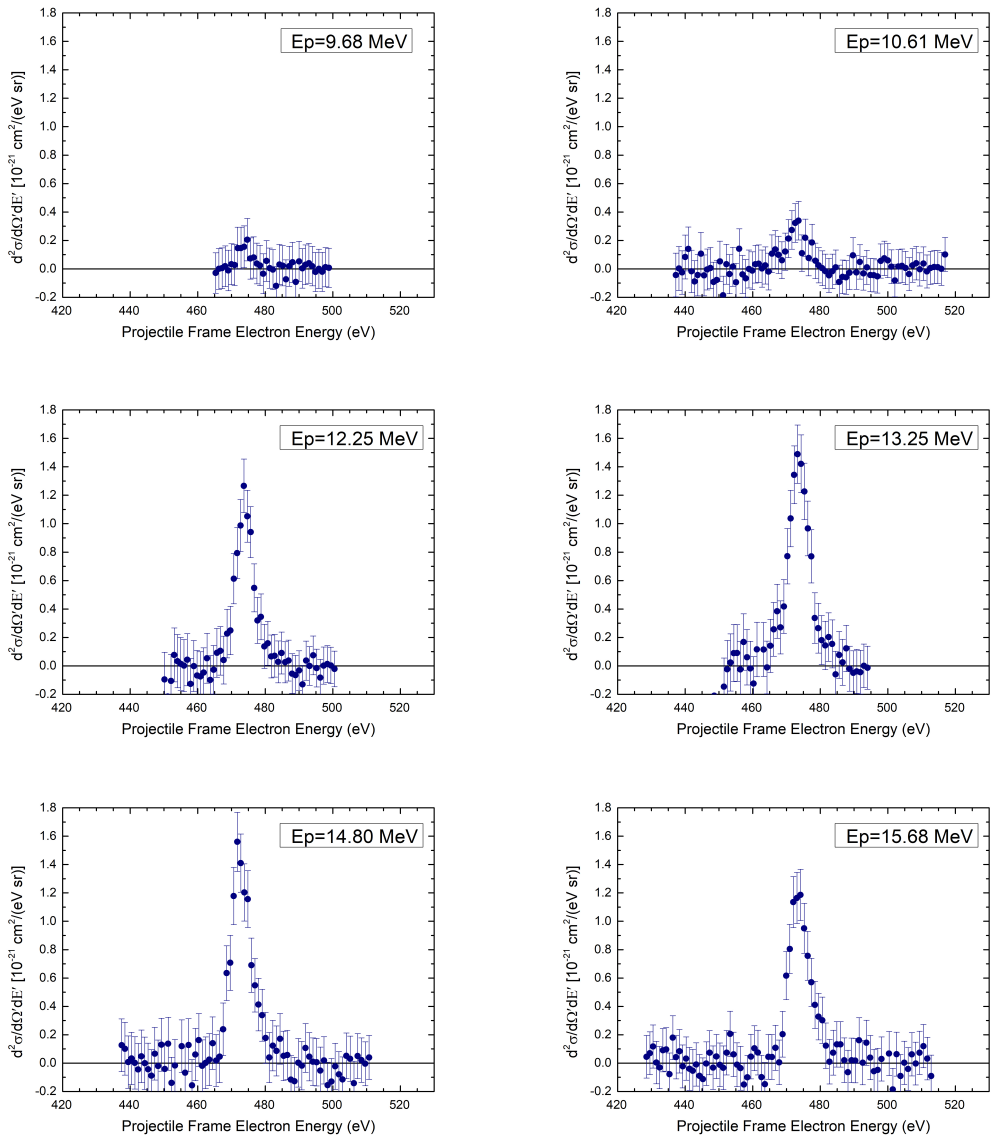

Figure 5.6: DDCS Auger electron spectra (background subtracted) showing the $2p^2\,{}^1D$ RTE peak for the collision system of Ep(MeV) $O^{7+}(1s)$ + H_2.

By integrating the area under each peak we can calculate the Single Differential Cross Section (SDCS). This way, we can compare our experimental data with the IA-RTE theory and the 3eAOCC theory. The theoretical values for the IA-RTE and the experimental data for collisions of O^{7+} with He are shown in Fig. 5.7.

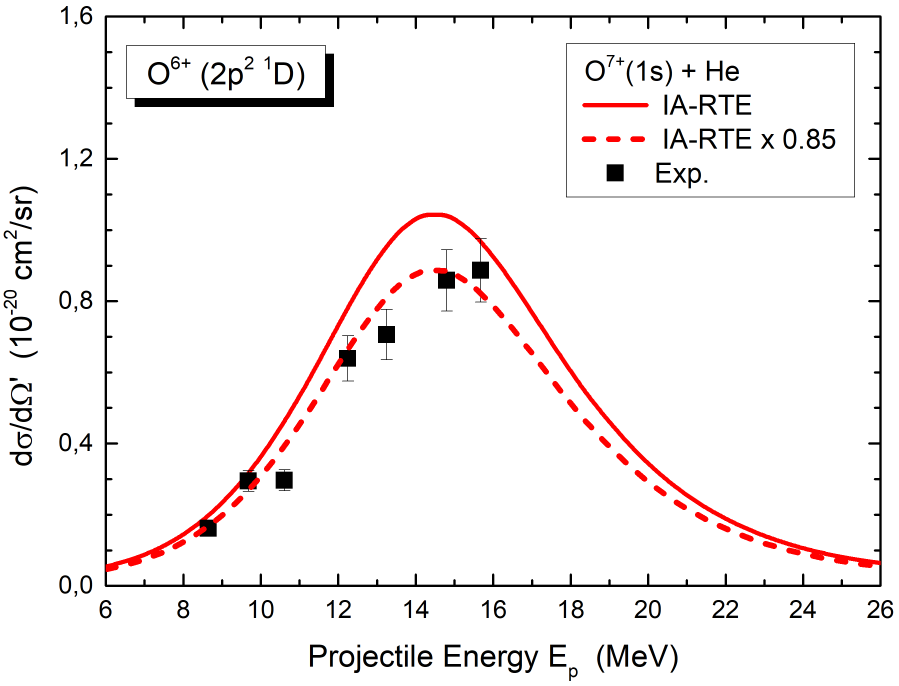

Figure 5.7: Solid back squares: SDCS for the $2p^2\,{}^1D$ RTE peak obtained after integrating the DDCS spectra of Fig. 5.3 for the collision system O^{7+} + He. Solid red line: IA-RTE theory. Dashed red line: IA-RTE theory scaled to best fit the experimental SDCS.

It is obvious that the theory does not reproduce accurately the experimental data. In fact, IA-RTE theory has to be scaled (multiplied by 0.85) in order to best fit the experimental data. This multiplicative factor is to be expected since IA-RTE is a model and not an ab initio theory.

The same problem appears also in the case of H_2. The theory has to be scaled by the same factor in order to fit with the experimental data, as shown in Fig. 5.8.

The comparison of the 3eAOCC theory, the IA-RTE results and the experimental data are shown in Fig. 5.9. 3eAOCC theory has no scaling and it seems to reproduce the experimental data quite adequately. In addition the contributions from the various final states of the target (ground state or excited state) are also depicted. There is a problem with the RTE energy peak which seems to be shifted to lower values than the experimental one. However, to reach such a conclusion we would need the measurements for higher collision energies which we did not have at the time of the experiments.

The success of the 3eAOCC theory in describing the TE process has been re-

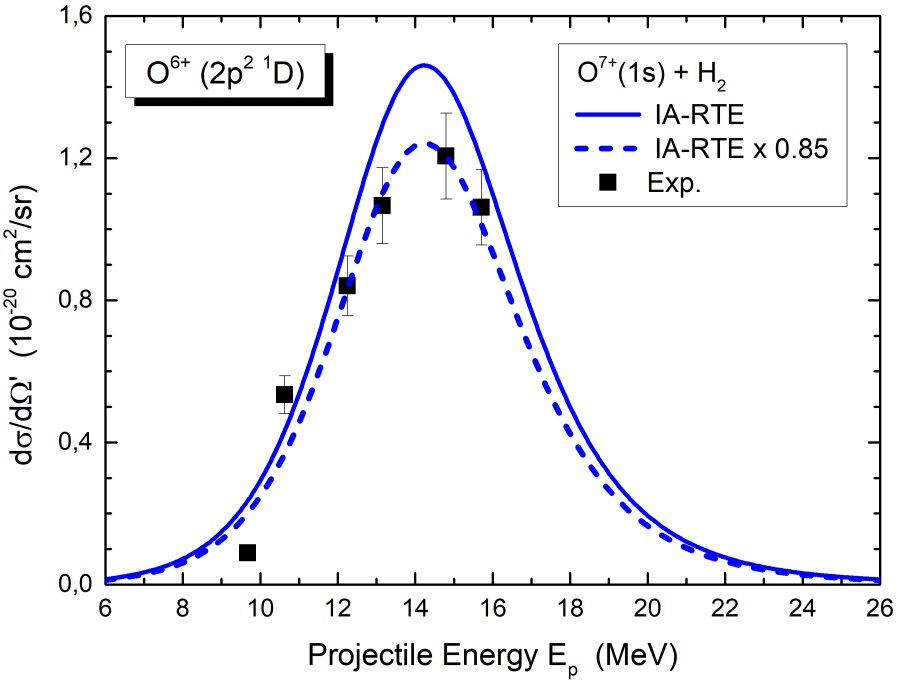

Figure 5.8: Solid back squares: SDCS for the $2p^2\,{}^1D$ RTE peak obtained after integrating the DDCS spectra of Fig. 5.6 for the collision system O^{7+} + H_2. Solid blue line: IA-RTE theory. Dashed blue line: IA-RTE theory scaled to best fit the experimental SDCS.

ported in [65] but for collisions involving He-like ions and He targets. Here we attempted to examine this success in H-like ions, thus involving three-electron collision systems which provide more stringent tests for the theory.

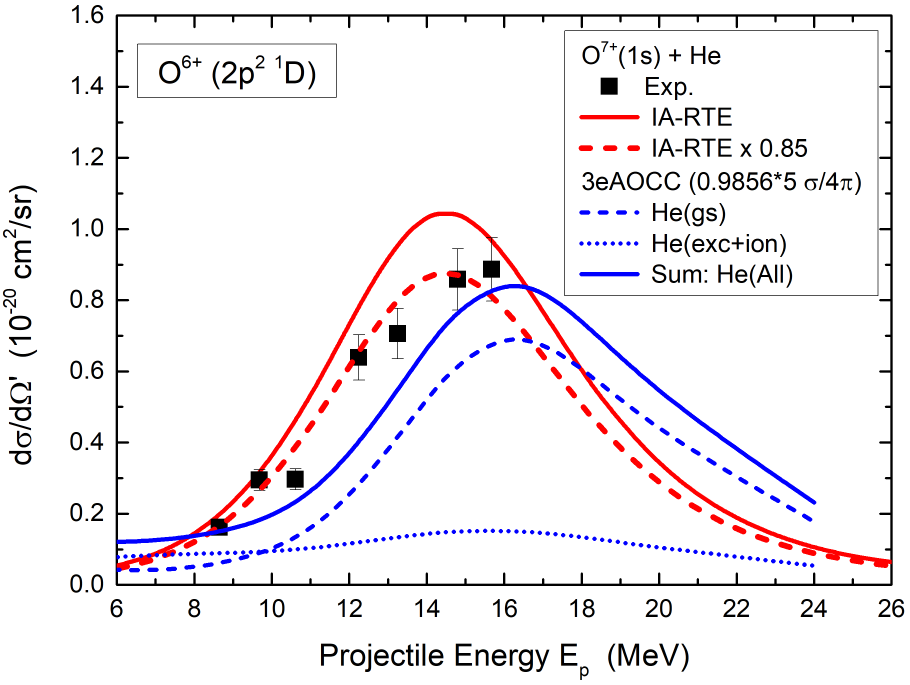

Figure 5.9: Solid back squares: SDCS for the $2p^2\,{}^1D$ RTE peak obtained after integrating the DDCS spectra of Fig. 5.3 for the collision system O^{7+} + He. Solid blue line: IA-RTE theory. Dashed blue line: IA-RTE theory scaled to best fit the experimental SDCS. Blue dashed line: 3eAOCC theory with He in ground state after collision. Blue dotted line: 3eAOCC theory with He in excited state or ionized after collision. Blue solid line: 3eAOCC theory with He in any state after collision.

Part II

The Toroidal Spectrometer

Chapter 6

The Electron Spectrometer

Another spectrometer was examined in this thesis. The toroidal electrostatic spectrometer which was transferred to the University of Ioannina from the GSI research center in Germany.

The choice of an electrostatic spectrometer over a magnetic one was made as it would analyze electron beams with energies lower than 20 keV. In this case, achieving such low magnetic fields that they are not disturbed by the Earth's magnetic field is extremely difficult. For this reason, the design of an electrostatic spectrometer was preferred. The biggest advantage of this toroidal spectrometer is that it not only analyzes the energy of the electron beams, but also provides information about the emission angle of the electrons.

Earlier cylindrical and spherical spectrometers such as those of Engelhardt *et al.* [66], Smeenk *et al.* [34] and Leckey *et al.* [67] led to a new spectrometer by Flexman *et al.* [68], based on theoretical work by Wollnik [69]. Based on this model Prof. Siegbert Hagmann designed and developed the present toroidal spectrometer. A two times smaller prototype of this was used as a trial by A. Bohris and B. Bathelt during their dissertations under the supervision of S. Hagmann. A few years later, Zäpfel used a spectrometer of this type in real size, again under the supervision of S. Hagmann.

6.1 Technical Characteristics and Properties

6.1.1 Geometrical Characteristics

The spectrometer consists of two main parts. The energy analyzer and the lens. As shown in Fig. 6.1 the energy analyzer consists of two parallel surfaces, named as toroidal electrodes. Both of them have toroidal geometry, creating this way a free zone between them. A shielded, grounded aluminium cylinder creates a cylindrical field-free target zone inside the spectrometer, where the target can be placed. The transition from the target zone to the energy analyzer is through a 10 mm slit, milled

into the aluminium cylinder. The slit is reduced to 3 mm by another slit for better energy and angular resolution.

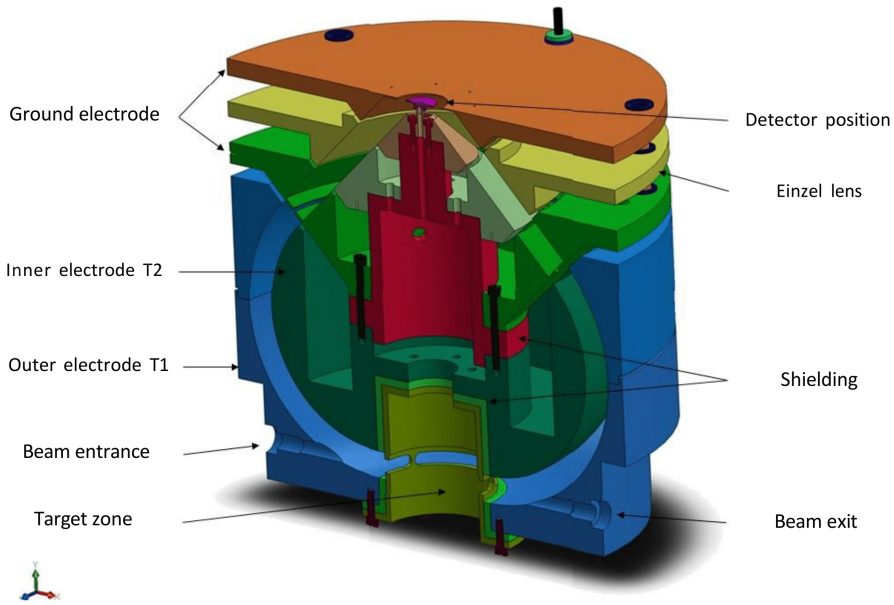

Figure 6.1: 3D CAD view of the toroidal spectrograph.

The orientation of the spectrometer with respect to the beam axis is perpendicular to it. In the lower part of the image are shown the two 10 mm diameter openings used for the passage of the beam. The beam enters through one hole in the interaction region and exits through the other hole after colliding with the target. The target electrons are emitted into the angular elements $\Delta\theta$ and $\Delta\phi$ and their energy is analyzed by the electric field. The polar angle θ is defined based on the beam axis and due to the symmetry of the spectrometer its entire range is covered. The azimuthal angle $\Delta\phi$ is defined by the 3 mm entrance slit. As shown in Fig. 6.2 the distance between the center S and the entrance slit S$'$ is 39 mm and defines the accepted azimuthal angle. For this toroidal spectrometer the acceptance azimuthal angle $\Delta\phi = \pm$ 38.5 mrad or 2.2°. The values of all the geometrical parameters of the toroidal spectrometer are presented in Tab. 6.1

Emitted electrons from the target travel in straight paths in the field-free target zone. The energy analyzer double-focuses them, making sure that the polar angle of electrons with the pass energy remains the same after passing through. Also, due to the rotational symmetry there is no electrostatic force acting perpendicularly on the electrons path. The spectrometer is completely covered with a double layer of μ - metal to reduce the effects of the earth's magnetic field.

6.1.2 Optical Properties

The calibration or spectrometer constant f_{spec} is defined as the ratio between the analysis voltage U and the electron energy E and depends only on the analyzer's geometry. The toroidal analyzer's geometry combines elements of both spherical

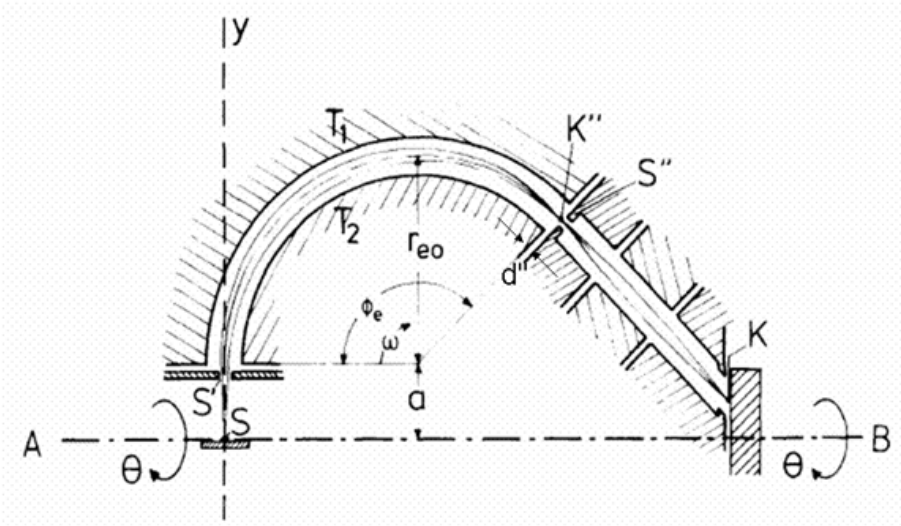

Figure 6.2: Schematic representation of the toroidal spectrometer in half-section along the rotation axis AB (symmetry axis). The trajectories of the transmitted monochromatic electrons emitted from a point source are also shown. T_1 and T_2 — outer torus and inner torus. r_{e0} — mean radial curvature radius of the target trajectory. α — cylinder radius. Φe — analyzer sector angle. S — target focal spot (object). S′ — entrance slit at the object. S″ — exit slit at the image. K″ — imaging circle after the analyzer section. d″ — distance between the exit slit and the end of the analyzer sector. K — imaging circle at the position of the detector. Taken from [10].

and cylindrical analyzers, defined by cylindrical and spherical radii (a and r_{e0}). Two limiting cases arise: $c = a/r_{e0} = 0$, resembling a spherical analyzer, and $c = a/r_{e0} = \infty$, resembling a cylindrical analyzer. Spherical analyzers are doubly focusing, unlike cylindrical ones, and toroidal analyzers inherit properties of both. The toroidal sector field has two curvature radii, influencing its electron-optical behavior.

Optimization of the toroidal spectrometer involves carefully selecting the curvature radii and sector angle, typically driven by resolution needs for both point-like and extended sources, such as a 5 mm gas jet. The spectrometer exhibits two key focusing properties: parallel-to-point, where particles emitted from the source parallel to each other and at the same emission angle onto the detector, and point-to-point, where particles from a common source point with emission angle θ but different azimuthal angles ϕ are focused onto a common point with azimuthal angle acceptance $\pm\ \Delta\phi$. A sector angle (Φ_e) of 120 ° and 150 ° was calculated for each case respectively. For optimal focusing, a sector angle of 135° was chosen as a compromise between the ideal angles calculated for both focusing types. The relationship between Φ_e and the ratio c is crucial for optimizing focusing, as demonstrated in the literature.

Table 6.1: Geometrical parameters of the toroidal spectrometer at UoI.

Symbol	Description	Value
r_1	Outer radial curvature radius	110 mm
r_2	Inner radial curvature radius	90 mm
r_{e0}	Curvature radius of the mean desired path	100 mm
a	Cylinder radius	50 mm
c	$c = \frac{a}{r_{e0}}$	0.5
p	Toroidal parameter $p = \sqrt{2 - \frac{2}{c\pi+2}}$	1.20
Φ_e	Analyzer sector angle	135° (2.36 rad)
s	Focal spot diameter	0.44 mm
s'	Width of the entrance slot	3 mm
s''	Width of the exit slot	3 mm
d''	Distance between sector end and image plane (on the exit slot)	4 mm
$d_{K''}$	Diameter of the image circle at the end of the analyzer sector	236 mm
d_K	Diameter of the image circle on the detector	20 mm

Energy Analyzer

Spectrometer Constant: Under the assumption that the angle ω (where $0 \leq \omega \leq \Phi$) is independent of the electric field, the toroidal electrodes potentials U_1 and U_2 are given as [70, 71]

$$U_{1,2} = \frac{E}{\pi a}(\pi a + 2r_{e0}) \ln \left[\frac{r_{e0}(2r_{1,2} + \pi a)}{r_{1,2}(2r_{e0} + \pi a)} \right]. \tag{6.1}$$

U_1 is the potential applied on the outer electrode T_1 with radius r_1 and U_2 is the potential on the inner electrode T_2 of radius r_2. It was calculated [72] that for pass energy of $E = 1000\ eV$, $U_1 = -185.55\ V$ and $U_2 = 216.96\ V$, leading to a spectrometer factor of $f_{spec} = 4.97\ eV/V$. The magnitude of the potentials is not exactly 200 V, but slightly asymmetric around 0 and adjusted to scan an energy range [73]. It is clear from the potential values that the ground potential is not in the center between the two electrodes, resulting to a very small energy shift. Simulations run on SIMION show that the calibration constant is 5.06 eV/V [73]. Measurements of Auger lines with this spectrometer confirmed a value of 5.12 eV/V for the calibration factor [10], and this is the adopted value.

Energy Resolution: The energy resolution according to calculations [70, 71] is given as

$$r_E = \frac{\Delta E}{E} = \frac{s'' + s' \cdot |M_r|}{2D_i \cdot r_{e0}}, \tag{6.2}$$

where the radial magnification M_r is

$$M_r = \cos(p \cdot \Phi_e) - \frac{d''}{r_{e0}} p \sin(p \cdot \Phi_e). \tag{6.3}$$

The energy dispersion is calculated as

$$D_i = \frac{1 - \cos(p \cdot \Phi_e)}{p^2} + \frac{d''}{r_{e0}} \frac{\sin(p \cdot \Phi_e)}{p}. \tag{6.4}$$

Angular Resolution: The ion beam axis is perpendicular to the axis of the rotational symmetry. The electron emission is recorded simultaneously under all polar angles θ, while the azimuthal angle range $\Delta\phi$ is kept small.

Polar Angle Resolution: The polar angle resolution $\Delta\theta$ after the analyzer part (from S' to S'') is determined by the axial size of the image s_r and by the diameter of the image circle $d_{K''}$ which is 236 mm. The axial image size itself, depends on the size of the focal spot, the axial magnification by the analyzer at the position of the exit slit and the polar angle θ, at which the focal spot is projected onto the circle k''. The polar angle resolution is calculated as

$$\Delta\theta = \frac{360^\circ s_r}{2\pi d''_K} \quad , \tag{6.5}$$

where

$$s_r = sM_z \cdot \cos(\theta) \tag{6.6}$$

and the axial magnification M_z is given by

$$M_z \approx \cos(q\Phi_e) - \frac{d''}{r_{e0}} \cdot q \cdot \sin(q\Phi_e). \tag{6.7}$$

Factor q is a geometric factor defined by the ratio of the radial to axial radius as

$$q = \frac{2}{\pi c + 2}, \tag{6.8}$$

For q = 0.75, $M_z = 0.22$. This means that for s = 0.44 mm the polar angle resolution is $\Delta\theta < \pm 0.023^\circ$. The real polar resolution was calculated as $\Delta\theta < \pm 0.28^\circ$, which is still acceptable.

Azimuthal Angle Resolution: The accepted azimuthal angle range $\phi_0 - \Delta\phi \leq \phi \leq \phi_0 + \Delta\phi$ is determined by the width of the entrance slit s' and the size of the focal spot at a defined distance h between the target and the entrance slit. The entrance aperture is smaller than the spectrometer acceptance, and the focal spot is much smaller than the distance to the entrance h, so the azimuthal angle resolution is determined by the azimuthal angle acceptance as

$$\Delta\phi = \pm 2.2^\circ. \tag{6.9}$$

In this calculation we do not take under consideration the stray fields at the entrance and exit. Moreover, higher-order terms couple polar and azimuthal blurring, so the azimuthal angle resolution — for example, in cases of incomplete rotation of the image — can degrade the polar angle resolution. Finally, the residual magnetic fields and the nonlinearities of position reading by the PSD can change the azimuthal angle resolution.

Einzel Lens

After passing through the sector field, the monochromatic electron beam is first focused on the image plane and then diverges. This beam is focused onto the detector by the electric field of the Einzel lens. Optimal focusing is achieved when the absolute value of the negative lens voltage U_L is three times that of the analyzer voltage U, which can be expressed as $U_L = -3U$. For instance, at a transmission energy of $E = 1000\ eV$, the analyzer voltage $U_{1,2}$ is set to $\pm 200\,\mathrm{V}$, resulting in a lens voltage of 600 V. The lens voltage is synchronized with the adjustments made to the analyzer voltage, in order to analyze the electron energy spectrum. Additionally, the negative potential on the lens acts as a filter for lower energy electrons. This leads the background electrons, which pass through the exit aperture after multiple scattering events on the walls or are generated by scattering, to be suppressed.

6.2 Spectrometer Assembly

After receiving the spectrometer, we proceeded with its reassembly. The spectrometer chamber was thoroughly cleaned and its components carbon coated to reduce secondary electron emission. A new electrical installation was also necessary. Photographs of the spectrograph components, as well as the assembly process are presented in Fig. 6.3. The chamber was pumped by a Leybold turbovac 360 turbomolecular pump backed by a Leybold SC 15D mechanical pump reaching a vacuum of 8.3×10^{-7} mbar. The experimental setup of the toroidal spectrometer is shown in Fig. 6.4.

Figure 6.3: Photos of the spectrometer parts during the assembly. The parts of the spectrometer after the carbon coating procedure are shown in the top left image. In the bottom right image the fully assembled spectrometer is shown.

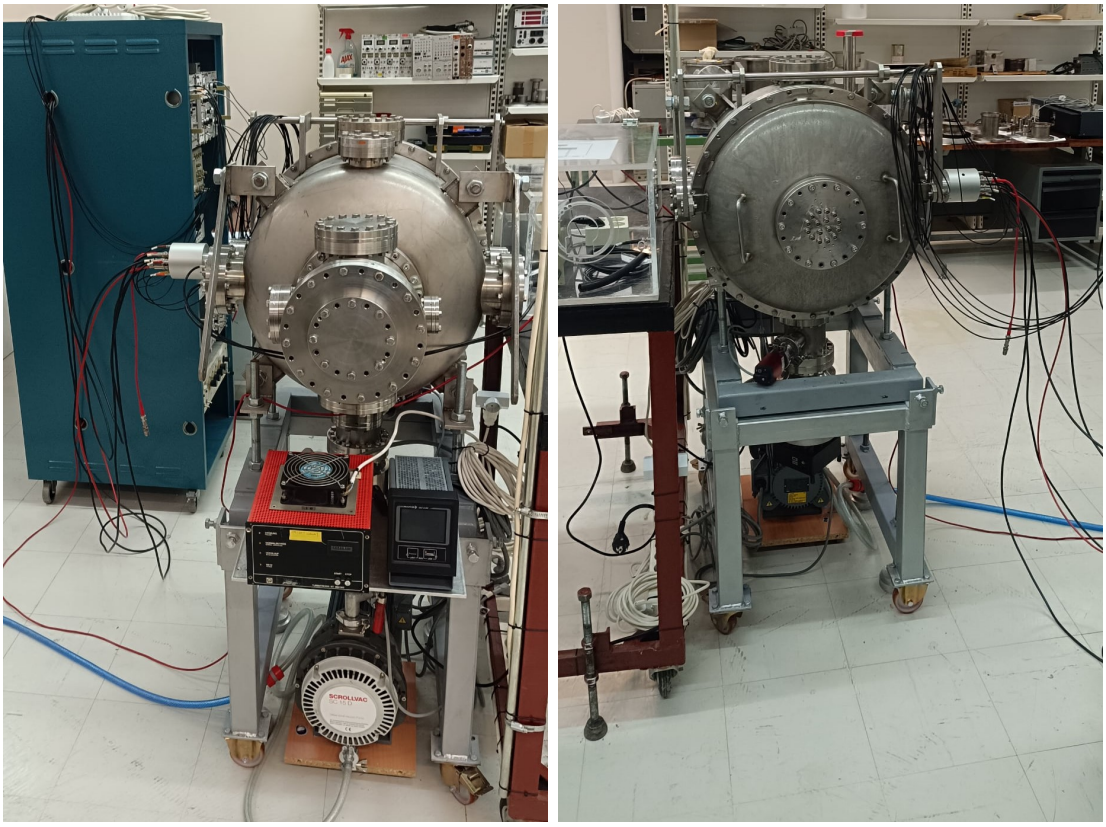

Figure 6.4: The experimental setup of the toroidal spectrometer. The spectrometer chamber and the vacuum manifold are shown in the photos.

Chapter 7

Electron Beams

For the experiments to be done with this spectrometer a stable electron source is required. In our case this stable source is an electron gun, providing intense mono-energetic electron beams. The structure and operation of the electron gun is described below.

7.1 Structure and Function of e-gun

A typical electron gun consists of four parts: the cathode, the Wehnelt cylinder, the anode and the electrostatic lens. Warming the cathode causes electron emission. The heating of the cathode is achieved by means of a filament through which a current flows. There are two types of cathodes: the direct ones, where the electron emission comes from the filament, which is parallel to the cathode, and the indirect ones, where the electron emission comes from heating a metal cylinder by using a filament. Indirect cathodes are superior to direct ones, since the cathode is at a constant potential and they produce a much larger number of electrons. The intensity of the electron beam is controlled by the Wehnelt cylinder. Electrons are attracted to the anode which is positively charged relative to the cathode. Finally, the electrostatic lens is responsible for focusing the electrons of the beam without changing their energy.

The charged particles are collected at the end by a Faraday cup. It is usually a conductive metal cylinder, the operation of which is independent of the mass and energy of the electron or ion beam that stops in it. The current collected is measured to determine the number of charged particles that hit it.

7.2 Electron gun characterization

For the electron gun characterization, a support base for it was built. The electron gun is mounted on a CF-63 flange. The electron guns used (shown in

Fig. 7.1) have ten pins and three cathodes, of which we used only one (central). In these e-guns there is also a built-in beam focusing system. 2D diagrams of the e-gun pins and the e-gun flange are shown in Fig. 7.2.

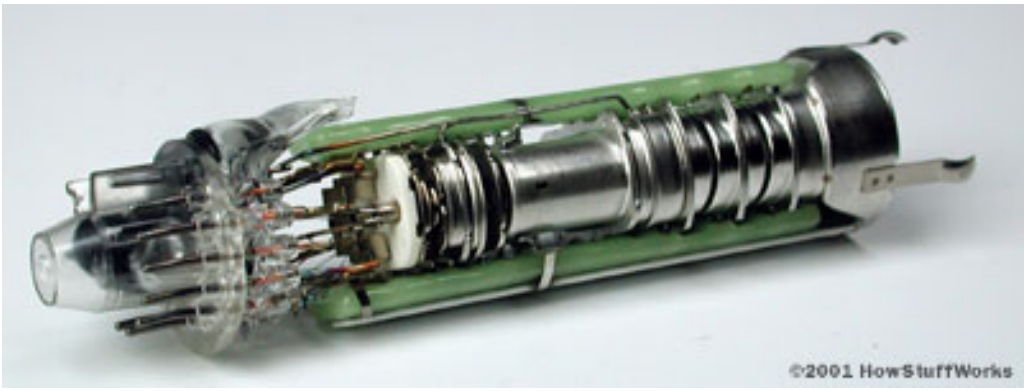

Figure 7.1: Photo of the electron gun used for the tests.

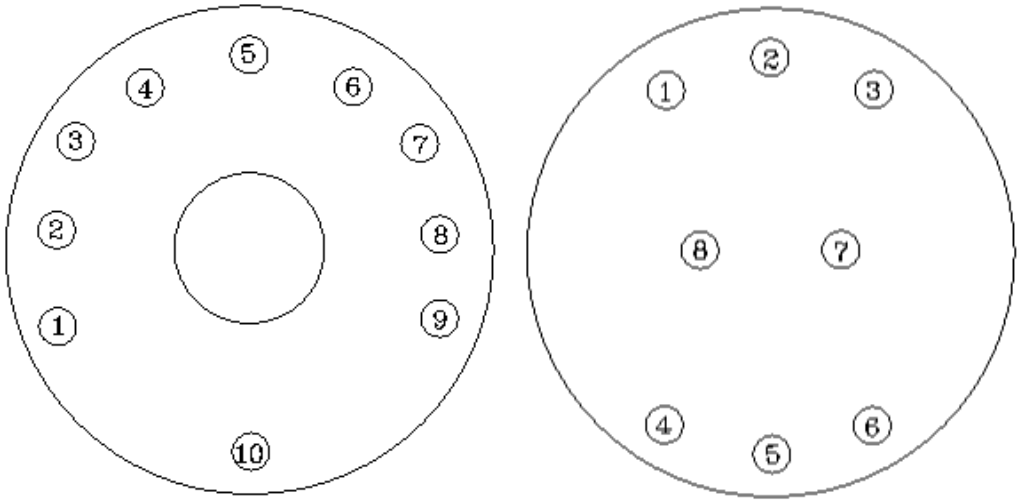

Figure 7.2: Left photo: e-gun back view. 1) Wehnelt electrode, 2) Wehnelt electrode, 3) central cathode, 4) anode, 5) second cathode, 6) filament 1, 7) filament 2, 8-9) third cathode, 10) Einzel lens. Right photo: e-gun mounting flange. 1) Wehnelt electrode, 2) central cathode, 3) anode, 4) second cathode, 5) filament 1, 6) filament 2, 7) third cathode, 8) Einzel lens.

Two power supplies as well as one current supply were used to operate the electron gun. The current supply SRS PS325/2500V-25W was connected to the filament. During the measurements we used only the central cathode. The other two cathodes, as well as the anode and the lens were grounded. The Wehnelt electrodes were connected to the TENNELEC TC952 power supply. The central cathode was connected to the Kethley high voltage supply 246. All elements of the e-gun have a different potential reference of absolute grounding (physical ground), the potential reference given to the cathode. Finally, the Faraday cup was connected to the Kethley picoammeter 6485 to measure the electrons current.

The filament should be slowly and steadily heated up to about 8 V before it is fully operational. After 6 V we begin to observe the presence of current in the

ammeter. Our goal was to generate current in the range from a few hundred nA to a few tens of μA, so we record the current values as a function of the filament, cathode and Wehnelt voltages.

As shown in Fig. 7.3 the current I_{FC} measured in the Faraday cup, without using the Wehnelt electrodes, can be increased by increasing the voltage V_C at the cathode. From the top right and bottom left graphs in Fig. 7.3, we see that applying voltage V_W to the Wehnelt electrodes reduces the current measured at the Faraday cup. In fact, from one voltage value onwards the current seems to be completely zeroed. Finally, as can be seen in the bottom right graph, for high voltages in the cathode and the Wehnelt electrodes the electron gun exhibits instabilities, as the current value oscillates. To achieve higher current values we can, in addition to increasing the cathode voltage V_C, increase the filament voltage V_F. For example, applying 7 V to the filament and -1000 V to the cathode reaches a current up to 150 μA, which is more than adequate for our future experiments.

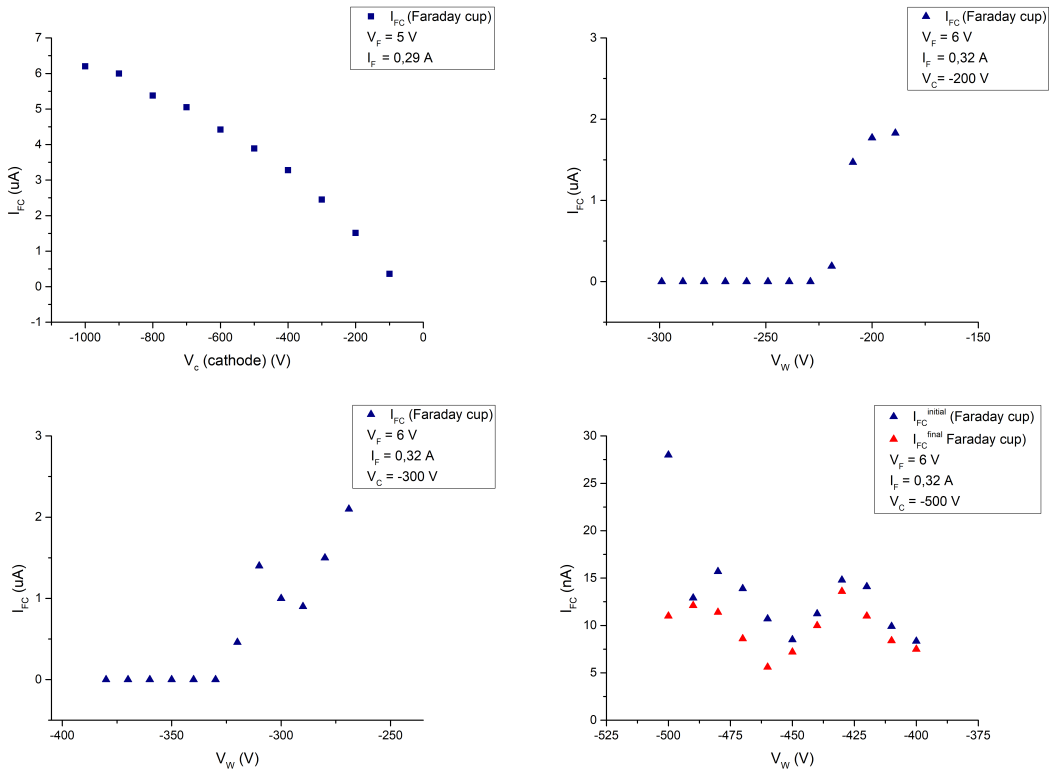

Figure 7.3: Top left: current measured in the Faraday cup without using Wehnelt electrodes. Top right: current measured in the Faraday cup using Wehnelt electrodes for $V_C = -200V$. Bottom left: current measured in the Faraday cup using Wehnelt electrodes for $V_C = -300V$. Bottom right: current measured in the Faraday cup using Wehnelt electrodes for $V_C = -500V$.

Chapter 8

Conclusions and Future Prospects

In this thesis we studied the process of transfer and excitation occurring during fast ion - atom collisions. The system studied was H-like oxygen beams, colliding with He or H_2 gas targets. From such collisions He-like $2p^2\ ^1D$ doubly excited oxygen ions are formed. Our research aimed to measuring the DDCS for these collisions. Our results were critically compared to the IA-RTE and 3eAOCC theories. IA-RTE model calculations have to be scaled by a factor of 0.85 to best fit the experimental data. 3eAOCC theory seems to reproduce the experimental data quite adequately providing also information about the contributions from the various final states of the target (ground state or excited state). However, due to the lack of higher collision energies, not offered by the accelerator, a full comparison with the measurements was not possible. The success of the 3eAOCC theory in describing the TE process has been reported recently in the literature but for collisions involving He-like ions and He targets. In this work we attempted to examine 3eAOCC in H-like ions, thus involving three-electron collision systems which provide more stringent tests for the theory.

In addition, a significant part of the work concerning the toroidal spectrometer was completed. In this work, the properties of this spectrometer are presented in detail, as well as the procedures that took place for its installation in the atomic physics laboratory of the University of Ioannina. Additionally, the analysis done on how to use an electron gun to be used as an electron source for the spectrometer in the future is presented.

This specific spectrometer is expected to increase the capabilities of the laboratory, as unlike the hemispherical one we have until now, this one can also study the angular distribution. In the next period of time, the study of the detector that will be used for the present arrangement will be completed and the spectrometer will be ready to be put into test operation. Upon completion of the tests for its characterization, this will be put into full operation that will make use of the laser infrastructure of the University of Ioannina or even be used in the NCSR "Demokritos" making use of ion beams.

Bibliography

[1] National Museums Scotland. Cockcroft-walton generator, . URL https://www.nms.ac.uk/explore-our-collections/stories/science-and-technology/cockcroft-walton-generator/.

[2] LBL News Magazine. history.aip.org, . URL https://history.aip.org/history/exhibits/lawrence/larger-image-page/radlab-cooksey-lawrence.htm.

[3] Felicie Albert, Alec Thomas, Stuart Mangles, S Banerjee, Sébastien Corde, A. Flacco, Michael Litos, D Neely, J. Vieira, Z Najmudin, Robert Bingham, Chandrashekhar Joshi, and T Katsouleas. Laser wakefield accelerator based light sources: Potential applications and requirements. *Plasma Physics and Controlled Fusion*, 56:084015, 07 2014. doi: 10.1088/0741-3335/56/8/084015.

[4] Mikhail Yavor. *Advances in Imaging and Electron Physics - Optics of Charged Particle Analyzers*. Elsevier, volume 157, 1st edition, 2009. ISBN : 9780123747686.

[5] Stefanos Nanos. *Mechanisms of electron capture and ionization in fast ion-atom collisions*. PhD thesis, University of Ioannina, 2023.

[6] Laoutaris Aggelos. *Excitation of heliumlike C^{4+} and O^{6+} projectile ions in collisions with He targets*. PhD thesis, University of Crete, 2024.

[7] E. P. Benis. *A novel high-efficiency paracentric hemispherical spectrograph for zero-degree Auger projectile spectroscopy*. PhD thesis, University of Crete, 2001.

[8] S. Harissopulos, M. Andrianis, M. Axiotis, A. Lagoyannis, A.G. Karydas, Z. Kotsina, A. Laoutaris, G. Apostolopoulos, A. Theodorou, T.J.M. Zouros, I. Madesis, and E.P. Benis. The tandem accelerator laboratory of ncsr demokritos: Current status and perspectives. *Eur. Phys. J Plus.*, 2021. doi: 10.1140/epjp/s13360-021-01596-5. URL Lhttps://doi.org/10.1140/epjp/s13360-021-01596-5.

[9] A. Laoutaris, S. Nanos, I. Madesis, S. Passalidis, E. P. Benis, A. Dubois, and T. J. M. Zouros. Coherent treatment of transfer-excitation processes in swift ion-atom collisions. *Phys. Rev. A*, 106:022810, Aug 2022. doi: 10.1103/PhysRevA.106.022810. URL https://link.aps.org/doi/10.1103/PhysRevA.106.022810.

[10] Natallia Lineba. *Emission niederenergetischer Elektronen in Stössen von schweren Ionen mit Festkörpertargets*. PhD thesis, Darmstadt Technical University, 2008.

[11] J. D. Cockcroft and E. T. S. Walton. Experiments with High Velocity Positive Ions. (I) Further Developments in the Method of Obtaining High Velocity Positive Ions. *Proc. Roy. Soc. Lond. A*, 136:619–630, 1932. doi: 10.1098/rspa.1932.0107.

[12] Ernest Lawrence – Facts. Nobel prize outreach ab. *NobelPrize.org.*, Mon. 17 Jun 2024. URL https://www.nobelprize.org/prizes/physics/1939/lawrence/facts/.

[13] M. Letournel. Brief review of the development of electrostatic accelerators and continuing work at strasbourg. In *Proceedings of the 1989 IEEE Particle Accelerator Conference, . 'Accelerator Science and Technology*, pages 1103–1106 vol.2, 1989. doi: 10.1109/PAC.1989.73366.

[14] Berkeley Lab. Bevatron site recognized for historical contributions to physics, . URL https://newscenter.lbl.gov/2021/06/25/bevatron-contributions-to-physics/.

[15] R. Geller. Electron cyclotron resonance sources: Historical review and future prospects (invited). *Review of Scientific Instruments*, 69(2):613–613, 02 1998. ISSN 0034-6748. doi: 10.1063/1.1148724. URL https://doi.org/10.1063/1.1148724.

[16] Toshiki TAJIMA. Laser acceleration and its future. *Proceedings of the Japan Academy, Series B*, 86(3):147–157, 2010. doi: 10.2183/pjab.86.147. URL https://www.jstage.jst.go.jp/article/pjab/86/3/86_3_147/_article.

[17] B. S. Nicks, T. Tajima, D. Roa, A. Nečas, and G. Mourou. Laser-wakefield application to oncology. *International Journal of Modern Physics A*, 34(34): 1943016, 2019. doi: 10.1142/S0217751X19430164. URL https://doi.org/10.1142/S0217751X19430164.

[18] P.-M. Hillenbrand, S. Hagmann, Y. S. Kozhedub, E. P. Benis, C. Brandau, R. J. Chen, D. Dmytriiev, O. Forstner, J. Glorius, R. E. Grisenti, A. Gumberidze, M. Lestinsky, Yu. A. Litvinov, E. B. Menz, T. Morgenroth, S. Nanos, N. Petridis, Ph. Pfäfflein, H. Rothard, M. S. Sanjari, R. S. Sidhu, U. Spillmann, S. Trotsenko, I. I. Tupitsyn, L. Varga, and Th. Stöhlker. Single and double k-shell vacancy production in slow $xe^{54+,53+}$-xe collisions. *Phys. Rev. A*, 105:022810, Feb 2022. doi: 10.1103/PhysRevA.105.022810. URL https://link.aps.org/doi/10.1103/PhysRevA.105.022810.

[19] William A. Reed. *NONDESTRUCTIVE TESTING AND INSPECTION USING ELECTRON LINACS*, pages 307–369. world scientific, . doi: 10.1142/9789814307055_0008. URL https://www.worldscientific.com/doi/abs/10.1142/9789814307055_0008.

[20] John A. Simpson. Design of retarding field energy analyzers. *Review of Scientific Instruments*, 32:1283–1293, 1961. URL https://api.semanticscholar.org/CorpusID:122064611.

[21] A. Ll. Hughes and V. Rojansky. On the analysis of electronic velocities by electrostatic means. *Phys. Rev.*, 34:284–290, Jul 1929. doi: 10.1103/PhysRev.34.284. URL https://link.aps.org/doi/10.1103/PhysRev.34.284.

[22] Heinrich Ewald and Helmut Liebl. Der astigmatismus des toroidkondensators. *Zeitschrift für Naturforschung A*, 10:872 – 876, 1955. URL https://api.semanticscholar.org/CorpusID:93107247.

[23] Edward M. Purcell. The focusing of charged particles by a spherical condenser. *Phys. Rev.*, 54:818–826, Nov 1938. doi: 10.1103/PhysRev.54.818. URL https://link.aps.org/doi/10.1103/PhysRev.54.818.

[24] H. Matsuda. Electrostatic analyzer with variable focal length. *Rev. Sci. Instrum.*, 32:850–852, 7 1961. doi: 10.1063/1.1717529. URL https://doi.org/10.1063/1.1717529.

[25] M. Jacka, M. Kirk, M. M. El Gomati, and M. Prutton. A fast, parallel acquisition, electron energy analyzer: The hyperbolic field analyzer. *Review of Scientific Instruments*, 70(5):2282–2287, 05 1999. doi: 10.1063/1.1149753. URL https://doi.org/10.1063/1.1149753.

[26] V V Zashkvara, M I Korsunskii, and O S Kosmachev. Focusing characteristics of an electrostatic mirror with a cylindrical field. *Zhurnal Tekhnicheskoi Fiziki (U.S.S.R.) For English translation see Sov. Phys. - Tech. Phys. (Engl. Transl.)*, Vol: 36, 1 1966.

[27] Frank Read. The parallel cylindrical mirror electron energy analyzer. *Review of Scientific Instruments*, 73:1129 – 1139, 03 2002. doi: 10.1063/1.1435841. URL https://www.researchgate.net/publication/234970249_The_parallel_cylindrical_mirror_electron_energy_analyzer.

[28] Afanas'evV.P. et al. "electrostatic energy analyzers for charged particle beams". ., (1978).

[29] Yu K Golikov, SN Davydov, and VV Korablev. Elektronnyy spektrometr s monokhromatizatsiyey zondiruyushchego potoka i uvelichennoy ploshchadyu skanirovaniya obraztsa electronic spectrometer with monochromatization of sounding flow and magnified area of sample scanning. *Pribory tech. eksperim*, 4:143–148, 1991.

[30] K Siegbahn, N Kholine, and G Golikov. A high resolution and large transmission electron spectrometer. *Nuclear Instruments and Methods in Physics Research Section A: Accelerators, Spectrometers, Detectors and Associated Equipment*, 384(2):563–574, 1997. ISSN 0168-9002. doi: https://doi.org/10.1016/S0168-9002(96)00719-X. URL https://www.sciencedirect.com/science/article/pii/S016890029600719X.

[31] V.D Belov and M.I Yavor. Two-stage systems with intermediate beam retarding for energy and spatial analysis of photoelectrons. *Nuclear Instruments and Methods in Physics Research Section A: Accelerators, Spectrometers, Detectors and Associated Equipment*, 427(1):197–202, 1999. ISSN 0168-9002. doi: https://doi.org/10.1016/S0168-9002(98)01524-1. URL https://www.sciencedirect.com/science/article/pii/S0168900298015241.

[32] Korsunskii O. S. Zashkvara V. V. and Red'kin V. S. Focusing properties of a toroidal electrostatic field. *Sov. Phys. Tech. Phys.*, 38(8):1336–1343, 1968.

[33] Khokhlov M. Z. and Remizov A. P. Electrostatic analyzers with symmetric angular characteristics for solar wind studies. *Kosmicheskije issledovanija (Space Studies)*, 7:459–462, 19689.

[34] R.G. Smeenk, R.M. Tromp, H.H. Kersten, A.J.H. Boerboom, and F.W. Saris. Angle resolved detection of charged particles with a novel type toroidal electrostatic analyser. *Nuclear Instruments and Methods in Physics Research*, 195(3): 581–586, 1982. ISSN 0167-5087. doi: https://doi.org/10.1016/0029-554X(82)90022-2. URL https://www.sciencedirect.com/science/article/pii/0029554X82900222.

[35] Andrey Trubitsyn. New electrostatic analyzer with angular and energy resolution. *Technical Physics Letters - TECH PHYS LETT*, 21:498–499, 01 1995. URL https://www.researchgate.net/publication/252279859_New_electrostatic_analyzer_with_angular_and_energy_resolution.

[36] N. J. Esponda, M. A. Quinto, R. D. Rivarola, and J. M. Monti. Dynamic screening and two-center effects in neutral and partially dressed ion-atom collisions. *Phys. Rev. A*, 105:032817, Mar 2022. doi: 10.1103/PhysRevA.105.032817. URL https://link.aps.org/doi/10.1103/PhysRevA.105.032817.

[37] M.E. RUDD and J.H. MACEK. Chapter 2 - mechanisms of electron production in ion—atom collisions. In E.W. McDANIEL and M.R.C. McDOWELL, editors, *Case Studies in Atomic Physics*, pages 47–136. Elsevier, 1974. ISBN 978-0-7204-0292-6. doi: https://doi.org/10.1016/B978-0-7204-0292-6.50006-6. URL https://www.sciencedirect.com/science/article/pii/B9780720402926500066.

[38] M E Rudd. Mechanisms of electron production in ion-atom collisions. *Radiat. Res., no. 1, pp. 153-180*, 10 1975. doi: 10.2307/3574175. URL https://www.osti.gov/biblio/4106628.

[39] J. Newcomb, T. R. Dillingham, James Hall, S. L. Varghese, Philip L. Pepmiller, and Patrick Richard. Electron capture by metastable projectiles on he and ne. *Phys. Rev. A*, 29:82–91, Jan 1984. doi: 10.1103/PhysRevA.29.82. URL https://link.aps.org/doi/10.1103/PhysRevA.29.82.

[40] I Madesis, A Laoutaris, S Doukas, A Dimitriou, E P Benis, and T J M Zouros. Separation and solid angle correction of the metastable 1s2s2p 4p auger yield produced in ion-atom collisions using the biased as cell technique: A tool for the determination of the population mechanisms. *Journal of Physics: Conference*

Series, 635(5):052082, aug 2015. doi: 10.1088/1742-6596/635/5/052082. URL https://dx.doi.org/10.1088/1742-6596/635/5/052082.

[41] E.P. Benis and T.J.M. Zouros. The hemispherical deflector analyser revisited: Ii. electron-optical properties. *Journal of Electron Spectroscopy and Related Phenomena*, 163(1):28–39, 2008. ISSN 0368-2048. doi: https://doi.org/10.1016/j.elspec.2008.02.001. URL https://www.sciencedirect.com/science/article/pii/S0368204808000030.

[42] E. Benis and Theo Zouros. The hemispherical deflector analyser revisited: Ii. electron-optical properties. *Journal of Electron Spectroscopy and Related Phenomena*, 163:28–39, 04 2008. doi: 10.1016/j.elspec.2008.02.001.

[43] M. Dogan, M. Ulu, G. G. Gennarakis, and T. J. M. Zouros. Experimental energy resolution of a paracentric hemispherical deflector analyzer for different entry positions and bias. *Review of Scientific Instruments*, 84(4):043105, 04 2013. ISSN 0034-6748. doi: 10.1063/1.4798592. URL https://doi.org/10.1063/1.4798592.

[44] Voikopoulos Spyridon. Production of fast high-charged iontic beams with stripping techniques. Master's thesis, University of Ioannina, 2021.

[45] O. Sise, G. Martínez, I. Madesis, A. Laoutaris, A. Dimitriou, M. Fernández-Martín, and T.J.M. Zouros. The voltage optimization of a four-element lens used on a hemispherical spectrograph with virtual entry for highest energy resolution. *Journal of Electron Spectroscopy and Related Phenomena*, 211:19–31, 2016. ISSN 0368-2048. doi: https://doi.org/10.1016/j.elspec.2016.05.004. URL https://www.sciencedirect.com/science/article/pii/S0368204816300573.

[46] D. Brandt. Resonant transfer and excitation in ion-atom collisions. *Phys. Rev. A*, 27:1314–1318, Mar 1983. doi: 10.1103/PhysRevA.27.1314. URL https://link.aps.org/doi/10.1103/PhysRevA.27.1314.

[47] T. J. M. Zouros, D. H. Lee, and P. Richard. Projectile 1s→2p excitation due to electron-electron interaction in collisions of o^{5+} and f^{6+} ions with h_2 and he targets. *Phys. Rev. Lett.*, 62:2261–2264, May 1989. doi: 10.1103/PhysRevLett.62.2261. URL https://link.aps.org/doi/10.1103/PhysRevLett.62.2261.

[48] H.-P. Hülskötter, W. E. Meyerhof, E. Dillard, and N. Guardala. Evidence for electron-electron interaction in projectile k-shell ionization. *Phys. Rev. Lett.*, 63:1938–1941, Oct 1989. doi: 10.1103/PhysRevLett.63.1938. URL https://link.aps.org/doi/10.1103/PhysRevLett.63.1938.

[49] P A Závodszky, G Tóth, S R Grabbe, T J M Zouros, P Richard, C P Bhalla, and J A Tanis. Forward-backward asymmetry in the inelastic scattering of electrons from highly charged ions. *Journal of Physics B: Atomic, Molecular and Optical Physics*, 32(18):4425, sep 1999. doi: 10.1088/0953-4075/32/18/303. URL https://dx.doi.org/10.1088/0953-4075/32/18/303.

[50] Jesse W. M. Dumond. The linear momenta of electrons in atoms and in solid bodies as revealed by x-ray scattering. *Rev. Mod. Phys.*, 5:1–33, Jan 1933. doi: 10.1103/RevModPhys.5.1. URL https://link.aps.org/doi/10.1103/RevModPhys.5.1.

[51] C. Kelbch, S. Hagmann, S. Kelbch, R. Mann, R.E. Olson, S. Schmidt, and H. Schmidt-Böcking. Observation of structures in the binary encounter peak in fast uranium-rare gas collisions. *Physics Letters A*, 139(7):304–307, 1989. ISSN 0375-9601. doi: https://doi.org/10.1016/0375-9601(89)90457-X. URL https://www.sciencedirect.com/science/article/pii/037596018990457X.

[52] P Richards, D H Lee, T J M Zouros, J M Sanders, and J L Shinpaugh. Anomalous q dependence of 0' binary encounter electron production in energetic collisions of fq+ (q=3-9) with he and h2 targets. *Journal of Physics B: Atomic, Molecular and Optical Physics*, 23(11):L213, jun 1990. doi: 10.1088/0953-4075/23/11/005. URL https://dx.doi.org/10.1088/0953-4075/23/11/005.

[53] Nicolás J. Esponda, Stefanos Nanos, Michele A. Quinto, Theo J. M. Zouros, Roberto D. Rivarola, Emmanouil P. Benis, and Juan M. Monti. Binary encounter electrons in fast dressed-ion–h2 collisions: Distorted wave theories and experiment. *Atoms*, 11(2), 2023. ISSN 2218-2004. doi: 10.3390/atoms11020017. URL https://www.mdpi.com/2218-2004/11/2/17.

[54] Zhensheng Tao, Cong Chen, Tibor Szilvási, Mark Keller, Manos Mavrikakis, Henry Kapteyn, and Margaret Murnane. Direct time-domain observation of attosecond final-state lifetimes in photoemission from solids. *Science*, 353(6294): 62–67, 2016. doi: 10.1126/science.aaf6793. URL https://www.science.org/doi/abs/10.1126/science.aaf6793.

[55] M. Clark, D. Brandt, J. K. Swenson, and S. M. Shafroth. Nonresonant electron transfer and projectile k-electron excitation in ion-atom collisions. *Phys. Rev. Lett.*, 54:544–546, Feb 1985. doi: 10.1103/PhysRevLett.54.544. URL https://link.aps.org/doi/10.1103/PhysRevLett.54.544.

[56] F. B. Rosmej, V. A. Astapenko, V. S. Lisitsa, and L. A. Vainshtein. Dielectronic recombination in non-LTE plasmas. *Matter and Radiation at Extremes*, 5(6): 064201, 10 2020. ISSN 2468-2047. doi: 10.1063/5.0014158. URL https://doi.org/10.1063/5.0014158.

[57] J. A. Tanis, E. M. Bernstein, W. G. Graham, M. Clark, S. M. Shafroth, B. M. Johnson, K. W. Jones, and M. Meron. Resonant behavior in the projectile x-ray yield associated with electron capture in s + ar collisions. *Phys. Rev. Lett.*, 49:1325–1328, Nov 1982. doi: 10.1103/PhysRevLett.49.1325. URL https://link.aps.org/doi/10.1103/PhysRevLett.49.1325.

[58] Till Jahnke, Uwe Hergenhahn, Bernd Winter, Reinhard Dörner, Ulrike Frühling, Philipp V. Demekhin, Kirill Gokhberg, Lorenz S. Cederbaum, Arno Ehresmann, André Knie, and Andreas Dreuw. Interatomic and intermolecular coulombic decay. *Chemical Reviews*, 120(20):11295–11369, 2020. doi: 10.1021/acs.chemrev.0c00106. URL https://doi.org/10.1021/acs.chemrev.0c00106. PMID: 33035051.

[59] Philip L. Pepmiller, Patrick Richard, J. Newcomb, R. Dillingham, J. M. Hall, Tom J. Gray, and M. Stockli. A study of transfer excitation in f8+ + he, ne and ar collisions. *IEEE Transactions on Nuclear Science*, 30(2):1002–1004, 1983. doi: 10.1109/TNS.1983.4332436.

[60] J. K. Swenson, Y. Yamazaki, P. D. Miller, H. F. Krause, P. F. Dittner, P. L. Pepmiller, S. Datz, and N. Stolterfoht. Observation of resonant transfer and excitation to specific ls-coupled states in o^{5+} + he collisions by high-resolution, 0° auger-electron spectroscopy. *Phys. Rev. Lett.*, 57:3042–3045, Dec 1986. doi: 10.1103/PhysRevLett.57.3042. URL https://link.aps.org/doi/10.1103/PhysRevLett.57.3042.

[61] W. Fritsch and C. D. Lin. Analysis of electron correlation in simultaneous electron transfer and excitation in atomic collisions. *Phys. Rev. Lett.*, 61:690–693, Aug 1988. doi: 10.1103/PhysRevLett.61.690. URL https://link.aps.org/doi/10.1103/PhysRevLett.61.690.

[62] H Bachau, R Gayet, J Hanssen, and A Zerarka. Transfer and excitation in ion-atom collisions at high impact velocities: a unified continuum distorted wave treatment of resonant and non-resonant modes in a four-body approach. ii. application to the collision s15+(1s)+h(1s). *Journal of Physics B: Atomic, Molecular and Optical Physics*, 25(4):839, feb 1992. doi: 10.1088/0953-4075/25/4/012. URL https://dx.doi.org/10.1088/0953-4075/25/4/012.

[63] T. J. M. Zouros. *Recombination of Atomic Ions*. NATO Advanced Study Institute Series B, 1992.

[64] Ashok Jain, R. Shingal, and T. J. M. Zouros. State-selective nonresonant transfer excitation in 50–400-kev $^3He^+$+h_2 and he collisions. *Phys. Rev. A*, 43:1621–1624, Feb 1991. doi: 10.1103/PhysRevA.43.1621. URL https://link.aps.org/doi/10.1103/PhysRevA.43.1621.

[65] A. Laoutaris, S. Nanos, A. Biniskos, S. Passalidis, E. P. Benis, A. Dubois, and T. J. M. Zouros. Projectile excitation to autoionizing states in swift collisions of open-shell he-like ions with helium. *Phys. Rev. A*, 109:032825, Mar 2024. doi: 10.1103/PhysRevA.109.032825. URL https://link.aps.org/doi/10.1103/PhysRevA.109.032825.

[66] HA Engelhardt, W Bäck, D Menzel, and H Liebl. Novel charged particle analyzer for momentum determination in the multichanneling mode: I. design aspects and electron/ion optical properties. *Review of Scientific Instruments*, 52(6):835–839, 1981.

[67] F. Toffoletto, R.C.G. Leckey, and J.D. Riley. Design criteria for an angle resolved electron spectrometer of novel toroidal geometry. *Nuclear Instruments and Methods in Physics Research Section B: Beam Interactions with Materials and Atoms*, 12(2):282–297, 1985. ISSN 0168-583X. doi: https://doi.org/10.1016/0168-583X(85)90064-3. URL https://www.sciencedirect.com/science/article/pii/0168583X85900643.

[68] FLEXMAN, J. H., WILLIAMS, J. F., and HAYES, P. A. Novel toroidal electrostatic electron energy analyser. *J. Phys. IV France*, 03(C6):C6–79–C6–89, 1993. doi: 10.1051/jp4:1993608. URL https://doi.org/10.1051/jp4:1993608.

[69] H. Wollnik. Second order transfer matrices of real magnetic and electrostatic sector fields. *Nuclear Instruments and Methods*, 52(2):250–272, 1967. ISSN 0029-554X. doi: https://doi.org/10.1016/0029-554X(67)90229-7. URL https://www.sciencedirect.com/science/article/pii/0029554X67902297.

[70] F. Toffoletto, R. C. G. Leckey, and J. D. Riley. Design criteria for an angle resolved electron spectrometer of novel toroid geometry. *Nuclear Instruments and Methods in Physics Research B*, 12:282, 1985.

[71] H. Wollnik. Focussing of charge particles. In A. Septier, editor, *Focussing of charge particles*, volume 2, pages 164–202. Academic Press, New York, 1967.

[72] U. Bechthold. *Dissertation*. PhD thesis, Universität Frankfurt/Main, 1996.

[73] Th. Zäpfel. *Dissertation*. PhD thesis, Universität Frankfurt am Main, 2001.